Formation Of Nanocoatings By Laser-Assisted Spray Pyrolysis And Laser Ablation On

2d Gold Nanotemplates

by

Gayan S. Dedigamuwa

A thesis submitted in partial fulfillment
of the requirements for the degree of
Master of Science
Department of Physics
College of Arts and Sciences
University of South Florida

Major Professor: Sarath Witanachchi, Ph.D.
Pritish Mukherjee, PhD.
George Nolas, PhD.

Date of Approval:
May 24, 2005

ACKNOWLEDGMENTS

I would like to thank Dr. Sarath Witanachchi, my supervisor for his suggestions and unwavering support. Everything I know about research has come from him. His vast experience and creativity helped me greatly along the way, and were essential to completion of this thesis. I would also like to thank Dr. P. Mukherjee for agreeing to serve as my faculty advisor, and providing advice when I needed it.

Further, I would like to thank Dr. Mathews and August for providing the AFM facilities where I needed some time in this project. Also I would like to thank all my lab mates specially Ted Wangensteen and Post Doc. Nagaraja Hosakoppa the assistant they gave me throughout the project.

And last, but not least, thanks to my parents Premadase and Jayanthi who encouraged me along and helped me through the difficult times.

TABLE OF CONTENTS

LIST OF FIGURES

**Formation of Nanocoatings by Laser-Assisted Spray Pyrolysis and Laser Ablation
on 2D Gold Nanotemplates**

Gayan S. Dedigamuwa

ABSTRACT

This thesis describes a new Laser-Assisted Spray Pyrolysis technique developed to grow nanoparticle coatings with controllable particle sizes. In this method, droplets of a precursor formed by a nebulizer are injected into a growth chamber using SF_6 carrier gas. An experimental study and a computational model to investigate the particle size dependence on various growth parameters have been carried out. The results show that heating of 1.5μm droplets of metalorganic precursor in a carrier gas using a CO_2 laser resulted in the formation of TiC and Fe_3O_4 particles with diameters in the range of 50-60nm. Also the results show that by reducing the concentration of the metal organic precursor the diameter of the deposited particles can be reduced.

In addition, we have investigated the formation of 2-D super lattices of gold nanoparticles on silicon substrate by using a technique called vapor-phase self-assembly, and have used this monolayer as a base coating for growth of TiC coatings with controlled grain sizes. The initial growth of TiC by laser ablation on heated templates indicates preferential nucleation of TiC on Gold Nanoparticles.

CHAPTER 1

INTRODUCTION AND BACKGROUND

1.1 INTRODUCTION

Thin film coating technology is now being strongly influenced by

nanotechnology. Nano-scale materials, characterised by grain sizes of less than 100nm

are being investigated and significant advances are being made for industrial use.

Thinking of small has been a global trend since the first calculator was built and nearly

filled a small room. Since then, how to make a product smaller, more portable, and easier

to manipulate and maneuver has been on the minds of innovators. But in recent years,

small has taken on a whole new dimension. Many developers are now thinking all the

way down to one-billionth of a meter- the nanometer.

A nanometer is 80,000 times smaller than the width of a human hair. When

controlling matter at this scale, different laws of physics come into play. The transition

from micro to nano can lead to a number of changes in physical properties. Two of the

major factors in this are the increase in the ratio of surface area to volume, and the size of

the particle moving into the realm where quantum effects predominate.

The increase in the surface-area to-volume ratio, which is a gradual progression,

as the particle gets smaller, leads to an increasing dominance of the behavior of atoms on

the surface of a particle over which of those in the interior of the particle. This affects

both the properties of the particle in isolation and its interaction with other materials.

High surface area is a critical factor in performance of catalysis and structures such as electrodes, allowing improvement in performance in devices such as fuel cells and batteries.

The large surface area of nanoparicles also results in substantial interactions between the intermixed matters in nanocomposites, leading to special properties such as increased strength and /or heat resistance, ultraviolet (UV) blocking, anti-static, and conductive capabilities. Paint and coating industries were among the first to take advantage of these capabilities. Companies also found that with the incorporation of nanoparticles and thin film nanocoatings have stronger bonds and better flexibility, with little cost differences. These coatings are smoother, stronger, and more durable. When used on products, the results range from scratch-resistant and self-cleaning surfaces to moisture-absorbing clothing.

Also it is well known that when the coating is composed of nanocomposites, the hardness of the coating is altered according to the Hall-Petch relation. The Hall-Petch relation describes the dependence of hardness (H_v) on the grain size in comparison to the conventional material. The relationship is as follows.

$$H_v = H_{v0} + kd^{-1/2} \quad \ldots\ldots\ldots (1.1)$$

Where H_{v0} and k are constant, d is the average size of the grains. This relationship has been confirmed in both theory and practice in many metallic materials.
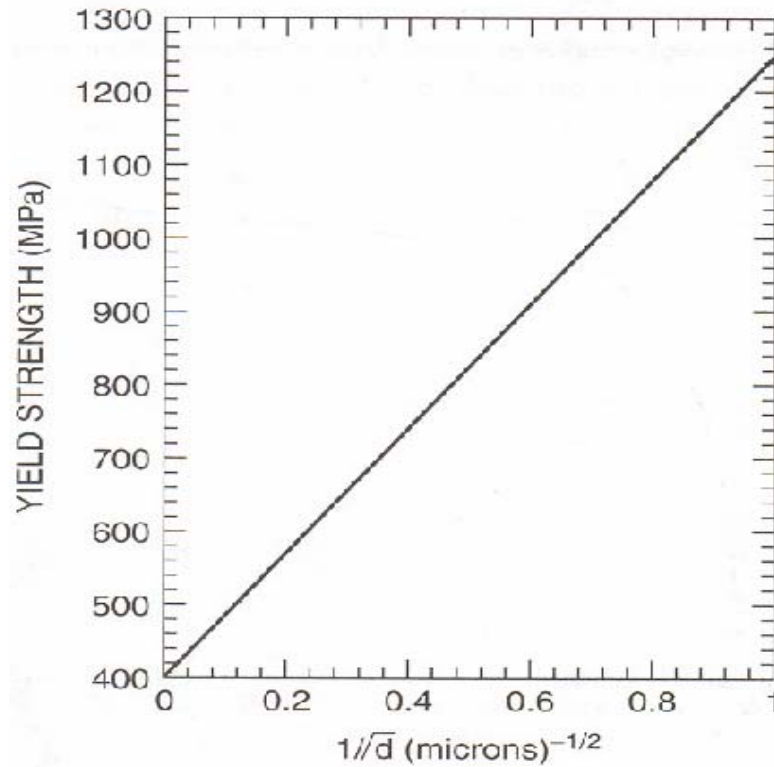
Figure 1.1: Yield strength of Fe-Co alloys $1/d^{1/2}$. (Adapted from C. H. Shang *et al*., *J. Mater. Res*. 15, 835, **2000**)

Figure 1.1 shows the measured Yield strength of Fe-Co alloys as a function of d. Assuming that the equation is valid for nanosized grains, a bulk material having 50nm grain size would have a yield strength of 4.14 Gpa. The reason for the increase in yield strength with smaller grain size is that materials having smaller grains have more grain boundaries, blocking dislocation movement. [1]

Additionally, the fact that nanoparticles have dimensions below the critical wavelength of light makes them transparent, a property which makes them very useful for applications in packaging, cosmetics and clear coatings.

These wide ranges of applications with nanoparticles and coatings have led to the development of a variety of methods and the growth techniques of making nanocoating. The growth techniques available in the industry can be mainly identified as physical and chemical synthesis. It can also be identified as bottom-up and top-down growth approach depending on the way that the coatings are being laid out on the substrate.

1.2 BOTTOM-UP APPROACH TO NANOSTRUCTURE GROWTH

The idea of this method is to create the assembly of nano-particles into well-defined two-dimensional arrays on the substrate. These 2D nanostructures are important because they have ultimate properties that can be critically determined by the topology and characteristic length scales of the network. Therefore, the control of the lateral ordering of the particles length scale appears the most challenging issue in this domain. Unlike micron size hard spheres, the organization of nanoparticles on a substrate is not simply entropy driven. Instead, interactions between particles, interaction between particle and substrate, and size distribution of the particles also play an important role in determining the packing morphology of the arrays. These challenges kept most of the researchers to work on other alternating methods such as top-down approaches. But recently, significant progress has been made to accomplish this task.

The first scientific approach in this sense has been reported at the beginning of 19th century. The scientists tried to make metal and gold nanoparticles in particular to cure ailments, although without understanding the exact nature of these particles. More recently though, a plethora of methods have been devised for the synthesis of gold [2,3], silver [4,5], platinum [6] and palladium [7,8] nanoparticles in variable sizes and shapes. In 1951,

4

Turkevich et al developed a method for the preparation of gold particles using citrate as the reducing agent, yielding stable nanoparticel solutions of low polydispersity. Hereafter, the solution will be referred to as polydisperse if the standard deviation exceeds 20% of the average value. Since the work of Turkevich, considerable effort has been devoted to developing new synthetic methods aiming at achieving better control of the size, the shape and the distance between the particles for the purpose of nanoparticle assembly. Following the basic principle of this method, different groups have successfully synthesized gold nanoparticles in colloidal form [9,10]. They used reduction of $HAuCl_4$ with trisodium citrate as the nucleating and reducing agent. By controlling concentration of reducing agent they have successfully showed that the particle size can be changed.

This is not the only method that has been developed in making nano particles with narrow size distribution. The reverse micelle [11] is also a well-known method that one can use. In this method, gold nano particles were prepared by the reduction of CTAB/octane +1-butanol/H_2O reverse micelle system using sodium tetrahydriborate ($NaBH_4$) as a reducing agent. A dodecanethiol ($C_{12}H_{25}SH$) was used to passivate the gold nanoparticles immediately after the formation of the gold colloid. By re-dispersing in toluene under ultrasonication, a supernatant containing nearly monodispersed dodecanethiol-capped gold nanoparticles were obtained. Even though this method is straightforward, the preparation of these chemicals should be very precise to get successful results.

5

1.2.1 MOLECULAR SELF ASSEMBLY

Molecular self-assembly is one of the techniques, which offers dimensional control in the deposition of nanoparticles of a fixed size on a substrate. Here, in this method the fabrication of a 2D array of nanoparticles on a suitable substrate largely depends on the size of the particles in a colloidal suspension. Since the polydispersity in particle size prevent the construction of well-defined arrays, the particle size distribution has to be narrow. Solution-based chemical routes, which are discussed in the above section, are ideally suited for producing mono-dispersed high purity nanomaterials with particle size tunability by adjustment of chemical concentration.

The first step towards controlled particle production is the initial isolation of species in the solution. Subsequently, a compound within the species is induced to decompose to desired material. If local separation is reached, the system spontaneously reaches a state of low energy by crystallization. The removal of excess solution prevents the continuous growth of the particles. The grown particles have a tendency to agglomerate slowly and loose their dispersion. Various organic surfactants that attach to surface molecules of the particles have been used to prevent particle agglomeration. These include fatty acids, alkyl thiols, alkyl disulfides, alkyl nitriles, and alkyl isonitrales. These surfactants posses end groups that attach to the surface of the particle, and steric repulsive methylene chains that are 8 to 12 units long. Under controlled conditions, the combination of Wan der Waals forces between the particles and dispersive forces cause the particles to self- assemble into closed- packed 2D superlattices.

1.2.2 LANGMUIR-BLODGETT TECHNIQUE

The LB technique for forming nanoparticles arrays is an important approach in which it is easy to control the preparation condition and to obtain uniform long-range order of nanoparticles. The LB-technique is one of the most promising techniques for preparing such thin films as it enables (i) the precise control of monolayer thickness, (ii) homogeneous deposition of the monolayer over large areas and (iii) the possibility to make multilayer structure with varying layer composition [12]. An additional advantage of the LB technique is that monolayers can be deposited on almost any kind of solid substrate. Deposition of films using the LB techique involves dipping a substrate through a monolayer of material on a water surface. If the substrate is hydrophobic, the hydrophobic ends of the molecules stick to the substrate as it is dipped through water. As the substrate is withdrawn, the hydrophilic ends of the monolayer stick to the hydrophilic ends of the deposited film. Using this technique multilayers can be manufactured.

1.2.3 DROP-CASTING TECHNIQUE (VAPOR-PHASE SELF-ASSEMBLING)

This appears to be the simplest technique for the formation of 2-dimensional arrays on a substrate. In this process, a drop of the colloidal nanoparticles is laid on the well-cleaned substrate and let the solvent evaporate slowly in a clean ventilated environment. As the solvent evaporates from the droplet, the particles in the solvent are likely to settle down on lowest possible energy on the substrate. The settlement of the particles on the substrate entirely depends on the size of the particles in colloidal form

and the physical forces among them. This method has proven very effective in creating sliver and gold 2D arrays. [13,14,15,16]

1.3 TOP-DOWN APPROACH TO NANOSTRUCTURE GROWTH

The ultimate idea of this technique is to get a uniform nanograined thin film on the substrate. The top-down growth technique is most straightforward method to fabricate a nanocoating.   Majority of the nanocoating growth techniques fall into this category. The main efforts have been to upgrade the quality of the films including the surface morphology, density and crystallinity. Among the several top-down growth methods available for the fabrication of thin films, chemical and physical vapor deposition processes are known to produce the best quality films [17]. These techniques enable precise control of the growth process, and have therefore been extensively used for growth of films for device applications. For applications that do not require high quality, a number of more economical techniques are available. These include electroplating [18], plasma spray [19] and screen- printing [20]. The simplicity, low capital cost of equipment, and the adaptability to large scale processing make these methods attractive for coating large surface areas. Apart from all, the most important issue in the coating industry is making films with controlled particle sizes. Even though above techniques (except CVD) are used in coating industries, still making nanocoatings with a narrow grain size distribution appears to be a big challenge.

The spray pyrolysis and chemical vapour deposition (CVD) are the popular techniques that have been developed and are being used to overcome this challenge.

These techniques are popular because they are easy to handle and suitable to be scaled up to industrialization and also they can be applied to wide variety of materials.

The main distinction between spray pyrolysis (SP) and CVD [21] techniques is the way the precursor materials reach the substrate surface. In CVD technique, precursor compounds impinge on the substrate in a vapor phase in such a way that a chemical reaction can take place as soon as (or even before) the substrate surface is reached. In the SP technique, usually liquid droplets splash the substrate, the temperature of the substrate evaporates the residual solvent leaving a dry precipitate, and a chemical reaction follows. However, whether or not the initial droplets really splash the substrate depends on the thermodynamic properties of the source solution that contains the material to be deposited. Indeed, if the solvent within the droplets is evaporated before they reach the substrate surface, the SP technique may lead to a growth process similar to that of chemical vapor deposition for nanoparticle coatings.

Here, in this work, two techniques for nanostructured film growth have been investigated. First, a laser-assisted spray pyrolysis technique was used, which is a top-down method, to deposit TiC and Fe_3O_4 nanoparticle coatings. The distribution of the particle sizes produced by this method and the ability to control the particle size by controlling the precursor concentration have been investigated.

Second, gold nanparticles were formed by using sodium citrate as the reducing agent (Turkevich method) and transferred to the silicon substrate by drop casting to form 2D arrays of templates. TiC films were deposited on these 2D templates to study the specific nucleation and subsequent growth.

9

The films deposited by both spray pyrolysis and laser ablation were characterized by X-ray diffraction and Atomic Force Microscope.

1.4 X-RAY DIFFRACTION ANALYSIS

X-ray powder diffraction (XRD) is one of the most powerful techniques for qualitative and quantitative analysis of crystalline compounds. The information obtained include types and nature of crystalline phases present, structural makeup of phases, degree of crystallinity, amount of amorphous content, size and orientation of crystallites.

When a material (sample) is irradiated with a parallel beam of monochromatic X-rays, the atomic lattice of the sample acts as a three dimensional diffraction grating causing the X-ray beam to be diffracted to specific angles. The diffraction pattern, that includes position (angles) and intensities of the diffracted beam, provides structural information about the sample.

1.5 ATOMIC FORCE MICROSCOPY ANALYSIS

"Atomic force microscopy (**AFM**) is a method of measuring surface topography on a scale from angstroms to 100 microns. The technique involves imaging a sample through the use of a probe, or tip, with a radius of 20 nm. The tip is held several nanometers above the surface using a feedback mechanism that measures surface–tip interactions on the scale of nanonewtons. Variations in tip height are recorded while the tip is scanned repeatedly across the sample, producing a topographic image of the surface. There are three different modes involving AFM. They are contact, tapping and non-contact. The basic modes of AFM operation are outlined below.[22]

Contact mode is one of the widely used scanning probe modes, and operates by rastering a sharp tip across the sample. An extremely low force (~10-9 N, interatomic force range) is maintained on the cantilever, thereby pushing the tip against the sample as it rasters. Either the repulsive force between the tip and sample or the actual tip deflection is recorded relative to spatial variation and then converted into an analogue image of the sample surface.

Tapping mode is the next most common mode used in AFM. When operated in air or other gases, the cantilever is oscillated at its resonant frequency (often hundreds of kilohertz) and positioned above the surface so that it only taps the surface for a very small fraction of its oscillation period. This is still contact with the sample in the sense defined earlier, but the very short time over which this contact occurs means that lateral forces are dramatically reduced as the tip scans over the surface. When imaging poorly immobilised or soft samples, tapping mode may be a far better choice than contact mode for imaging.

Non-contact operation is another method, which may be employed when imaging by AFM. The cantilever must be oscillated above the surface of the sample at such a distance that we are no longer in the repulsive regime of the inter-molecular force curve. This is a very difficult mode to operate in ambient conditions with the AFM. The thin layer of water contamination, which exists on the surface on the sample, will invariably form a small capillary bridge between the tip and the sample and cause the tip to "jump-to-contact"."

1.6 TITANIUM CARBIDE NANO-PARTICLE COATINGS

Titanium carbide (TiC) has been extensively used in many applications due to its interesting properties, such as very high melting point (melting temperature $\geq 3000^0$ C), high hardness, and thermal stability with excellent wear resistance, high oxidation resistance and low friction coefficient. [23] TiC coatings are widely used on metal cutting tools. TiC has also been utilized for diffusion barriers in semiconductor devices [24] and for thermal barrier coatings in fusion reactors [25]. Moreover it also can be used for coating steel bearings to reduce friction by exploiting the high yield stress of the coating. [26] A TiC coatings used in such applications is generally crystalline and, though fairly effective, may exhibit (under extreme chemical, thermal, and mechanical conditions) some of the shortcomings inherent to crystalline materials, in particular, grain-boundary corrosion and decohesion [27]. Hence, an amorphous, semimetallic, chemically inert, low-friction form of titanium carbide could represent a significant advance in materials engineering.

Amorphous films of TiC have been grown by metallorganic chemical vapor deposition (MOCVD) from titanium-coordination compound tris(2,2-bipyridine) titanium by Morancho and Ehrhard.[28] This approach was chosen because the molecules of metalorganic compounds dissociate at relatively low temperature, 200 to 500 ^{0}C, compared to the temperature of 1100 to 1350 ^{0}C that are required for crystalline TiC-film growth using precursors titanium tetrachloride, methane, and hydrogen [29].

We have used the titanium-coordination compound cyclopentadiethyltitanium trichloride in the Laser Assisted Spray Pyrolysis (LASP) process to deposit nanoparticle coating of TiC. This compound has a dissociation temperature close to 350 ^{0}C.

1.7 FERROUS OXIDE (Fe$_3$O$_4$) NANO-PARTICLE COATINGS

Magnetite, Fe$_3$O$_4$ is an extensively studied material due to its several interesting properties. Magnetite, Fe$_3$O$_4$ is a mixed-valence 3d transition metal oxide that has an inverse spinel structure (space group *Fd3m*) with a lattice constant of 0.8397 nm. The tetrahedral sites of the spinel structure are entirely occupied by Fe^{3+}, whereas the octahedral sites are occupied half by Fe^{2+} and half by Fe^{3+}. Fe$_3$O$_4$ undergoes a metal-to-insulator Verwey transition at 120 K and the Curie temperature of magnetite is 860 K.

Spintronic materials are currently receiving a lot of attention due to potential applications in giant magnetoresistive (GMR) devices such as magnetic field sensors, magnetoresistive random access memories (MRAM), read heads, and galvanic isolators. These devices require a source of spin-polarized electrons. As the GMR effect is originated from the spin dependent scattering near interface between magnetic and non-magnetic layers, it is possible to utilize half-metallic ferromagnets, in which the spin of electrons at Fermi surface is completely polarized. Magnetite, Fe$_3$O$_4$, is a promising source of spin-polarized carriers, because spin-resolved density of states calculations have suggested that electrons at the Fermi level are 100% spin polarized. Although experiments have not confirmed the predicted complete half-metallicity of Fe$_3$O$_4$, they do show that the number of minority electrons is much larger than the number of majority electrons at the Fermi level. Recently, GMR effects greater than 500% have been reported at room temperature for Fe$_3$O$_4$ nanocontacts.[30]

Although the fabrication methods as well as the physical properties of Fe$_3$O$_4$ were extensively studied in 1980s, the need for high storage density still provides considerable impetus to new fabrication technologies for obtaining Fe$_3$O$_4$ thin films, which serve as a

precursor for GMR devices. The response of GMR-based devices depends critically on the physical structure of the films, with parameters such as layer thickness, and chemical abruptness and roughness of the interfaces being crucial. In addition, transition of grain structure of polycrystalline Fe_3O_4 films from micro regime to nano regime is expected to alter the spin related magnetic properties. This comes about as a result of approaching single domain characteristics with decreasing grain size.

There have been many studies on synthesizing high quality Fe_3O_4 thin film and tunnel junctions using Fe_3O_4. A variety of techniques including molecular beam epitaxy [31], sputtering, [32] pulsed laser deposition and chemical synthesis have been used to deposit Fe_3O_4 films. We have used laser-assisted spray pyrolysis technique to grow nano-grained coatings of iron oxide. The size of the grains in the nano regime can be easily controlled by this method. The details of the growth process are presented in next chapters.

CHAPTER 2

SYNTHESIS OF TiC AND Fe$_3$O$_4$ NANOPARTICLE COATING BY LASER ASSISTED SPRAY PYROLYSIS

2.1 SPRAY PYROLYSIS

The spray pyrolysis technique is particularly interesting since it can be used to form coatings of variety of different materials. The main component of spray pyrolysis system is an atomizer that generates micro-droplets of precursor solution dissolved in a relatively volatile solvent. The droplets in the form of a fine spray are carried out of a nozzle onto a heated substrate by a carrier gas that can be inert or reactive. The constituents of the droplet decompose and react on the hot substrate to form the chemical compound. The substrate temperature should be high enough to evaporate the volatile solvents. The spray nozzle is usually scanned continuously during the growth to coat a large area of the substrate.

2.2 ULTRASONIC NEBULIZER

The sizes of the produced droplets depend on the technique used to atomize the solution. The simplest way to generate an aerosol spray is by a pneumatic process. In this method, the pressure drop at the orifice of a nozzle due to high flow gas causes the atomization of the solution. However, control of the particle size distribution produced by this method is very difficult. On the other hand, ultrasonic nebulizers are known to

produce a fairly uniform distribution of micrometer size droplets. Generally, the

nebulizer is operated at a frequency of 2.4MHz, where the precursor solution is converted

into a mist of particles in the range of 1-2μm in diameter. The diameter of the particle

has a dependency on the operating frequency of the nebulizer.

As produced these particles lack sufficient inertia and thus, have to be transported

by carrier gas. This gas flow is usually about 3 to 4 cc/s. Since the aerosol-generating

rate is independent of the flow rate, the transport of the droplets to the substrate can be

controlled without affecting the function of the nebulizer.

2.3 LASER ASSISTED SPRAY PYROLYSIS

This is a new technique that one can use to get finer and more concentrated

droplets of precursor compared to regular spray pyrolysis. The only difference is, the

droplets interact with a continuous wave (CW) CO_2 beam as they come out of the nozzle.

If the molecules of the precursor have a strong resonance absorption band at the

wavelength of the laser beam, the molecule is dissociated. This method has been

successfully used to form amorphous nanopartcles of Si/N/C [33]. However, use of this

method is restricted to compounds that have resonance absorption bands at an available

laser wavelength. This restriction is avoidable by introducing a carrier gas that has a high

absorption in the CO_2 wavelength. In this way, the laser energy is transfered to the
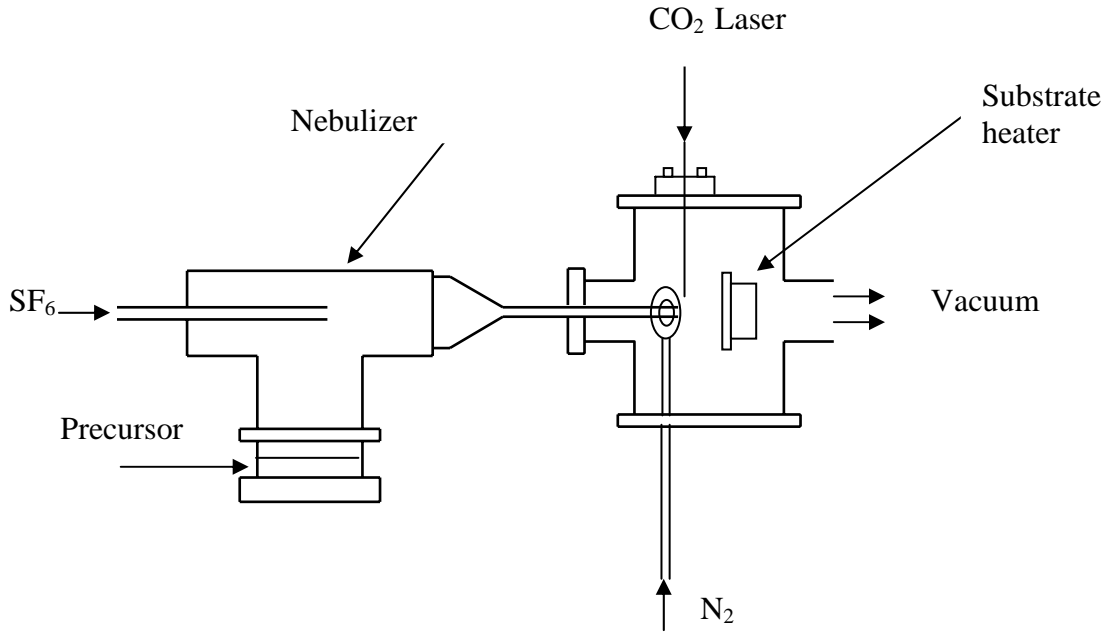
molecule in the form of heat.

2.4 PROCEDURE

Figure 2.1 Schematic diagram of the experimental setup.

The schematic diagram of the experimental apparatus is shown in fig 2.1. A deposition chamber was made of Glass. A CW CO_2 laser of 3W was focused to a point just above the funnel tube orifice. Since the proposed precursor does not have resonance absorption with CO_2 wavelength, sulfurhexafluoride (SF_6) is used as the carrier gas for aerosol transport. A CO_2 laser beam of wavelength 10.6μm was resonantly absorbed into the SF_6 molecules through vibrational excitation. Therefore, the carrier gas was heated by the CO_2 laser as the aerosol/gas mixture was injected into the chamber. The flow rate and thus the speed of the aerosol into the chamber were controlled by a gas flow meter. The pressure inside the chamber was kept very close to atmospheric. Also at the same time, the substrate was heated to promote film growth. When the droplets impinge upon

the heated substrate the subsequent film formation is dependant on the velocity of the drop, rate of reaction and the rate of evaporation of the solvent. At high velocities the droplets will flatten on the substrate leading to large particle sizes. On the other hand, if most of the solvent is evaporated when the drop gets to the substrate, the solid particles will stick to the substrate to form a crystallite smaller than the initial droplet. Therefore by adjusting the concentration of the solvent, the size of the particles depositing on the substrate can be controlled.

2.4.1 SYNTHESIS OF TITANIUM CARBIDE (TiC)

TiC nanoparticle coatings were synthesized by the laser assisted spray pyrolysis method. The precursor was prepared by dissolving the TiC containing organometallic compound, cyclopentadiethyltitanium trichloride ($C_5H_5TiCl_3$ crystalline from Alfa Aeser) in toluene with different concentrations. The Si(100) substrates were cleaned with an ultrasonic agitator in repeated baths of ethanol and acetone, then rinsed in high-purity deionized water and dried with nitrogen flow prior to loading into the chamber. Next, the prepared substrate was set up on the substrate holder 4cm away from the nozzle and the holder was heated to 350^0C. The nebulizer filled with precursor was setup as shown in fig 2.1. The chamber was continually pumped by a vacuum pump while nitrogen gas was injected to maintain the ambient pressure about 760mmHg. When the holder temperature reached $350\ ^0C$, the nebulizer was switch on. The process was run for 20min to get a good layer of TiC. Several samples were synthesized by changing the concentration.

2.4.2 SYNTHESIS OF FERROUS OXIDE (Fe_3O_4)

Fe$_3$O$_4$ nanoparticle coatings were synthesized by laser assisted spray pyrolysis method. The pentacarbonyliron (Fe (CO)$_5$ 99.5% from Alfa Aesar) in toluene based solution was used. All the parameters were kept as same as for titanium carbide synthesis. The process was run for 15min. Several samples were synthesized with precursor concentrations 0.05M, 0.1M, 0.2M and 0.25M.

CHAPTER 3

CHARACTERIZATION OF FILMS DEPOSITED BY SPRAY PYROLYSIS

3.1 CRYSTALLINITY OF NANOCOATINGS

X-ray diffraction (XRD) was performed on TiC and Fe_2O_3 samples. Since prepared samples were typically 800-2500A^o, a thin film attachment was used. The Scans were performed over $2\theta = 20\text{-}80^o$ for each sample. Fig 3.1, 3.2 and 3.3 respectively show TiC and Fe_2O_3 representative XRD patterns.
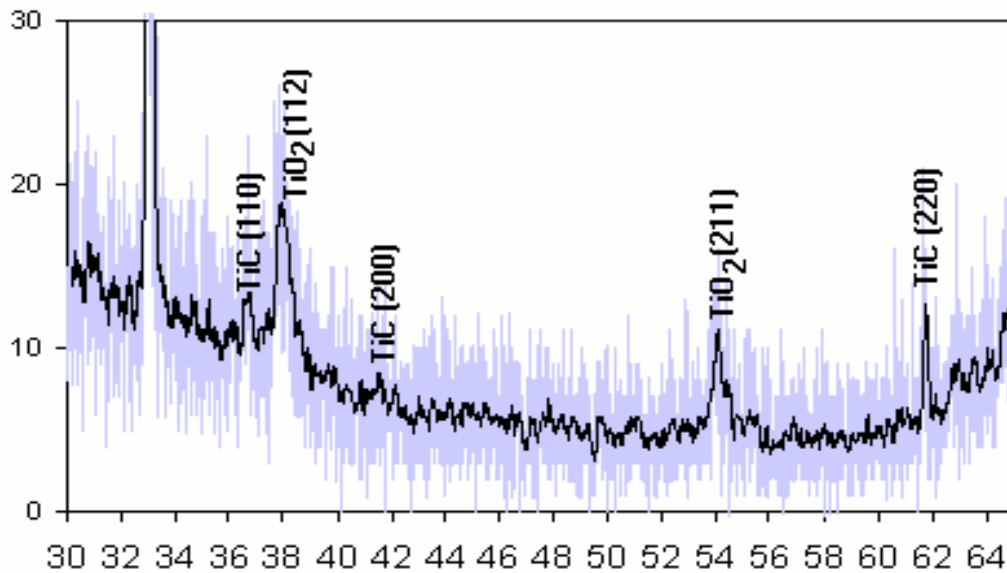

Figure 3.1: X-ray diffraction pattern of a TiC nanograined film deposited by spray pyrolysis without laser heating
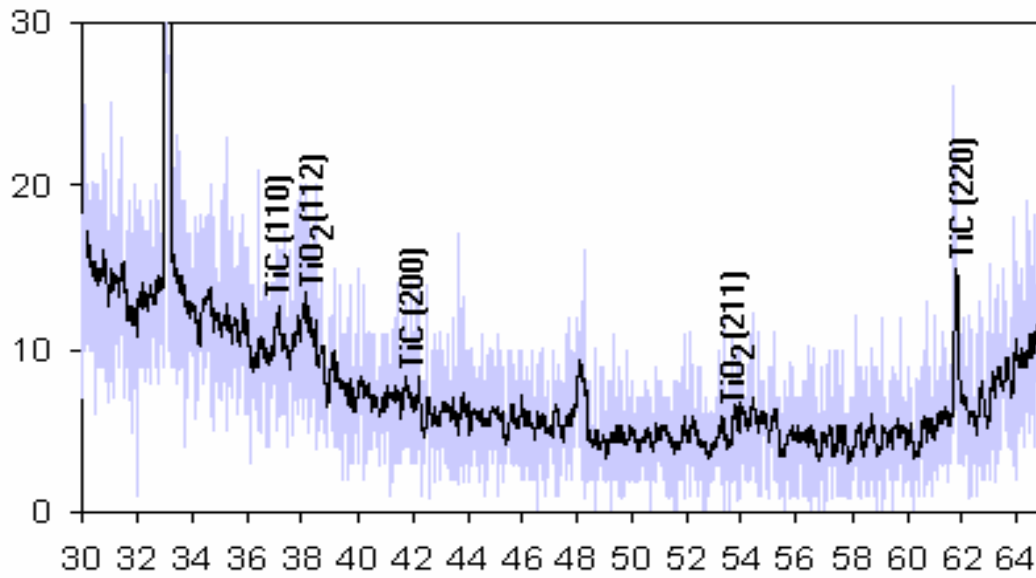
Figure 3.2: X-ray diffraction pattern of a TiC nanograined film deposited by spray pyrolysis with laser heating.

Fig 3.1 and 3.2 show the comparison of the XRD patterns of the TiC deposited on Si(100), which were made with and without a laser. Both indicate crystalline peaks of TiC (111), (200) and (220). Also it indicates the crystalline peaks of TiO_2 (112) and (211). The system currently in use for film growth is not high vacuum compatible, and thus, the deposited films are subjected to partial oxidation.
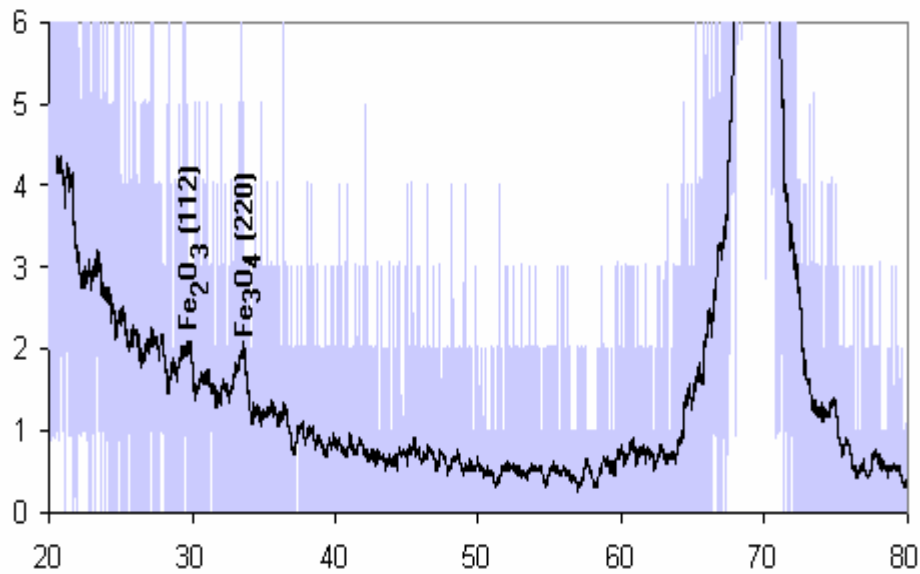
Figure 3.3: X-ray diffraction pattern of a Fe_3O_4 nanograined film deposited by spray pyrolysis with laser heating.

Fig 3.3 shows the XRD patterns of the deposited Fe_2O_3 on Si(100), which were made by using a laser. It indicates a crystalline peak of Fe_3O_4 (220). Also it indicates the crystalline peaks of γ-Fe_2O_3 (112). The intensity of the peaks is relatively low. Also it shows a XRD pattern of an amorphous structure. This peak can be eliminated and a pure film of Fe_3O_4 can be obtained by sealing the chamber for the oxygen.

3.2 EFFECT OF LASER HEATING ON NANOCOATINGS OF TiC

The laser heating of the droplets in spray pyrolysis technique can largely affect the surface morphology of the film. The laser heating in this process evaporates the solvent from the droplets and at the same time it decomposes the organomatallic precursor into the metal basics. As a result, the droplets shrink and become denser. Therefore the resultant coating consists of well-defined particles. The thin TiC films were analyzed by atomic force microscopy (AFM). An AFM image of a film deposited without laser heating is shown in (Fig 3.4). The average particle size is about 150nm. Irregular particle shapes and size are visible in the three dimensional image. In comparison, a film deposited with CO_2 laser heating of the carrier gas shows a distribution of well-defined particles (Fig 3.5). The average particle size is about 50nm.
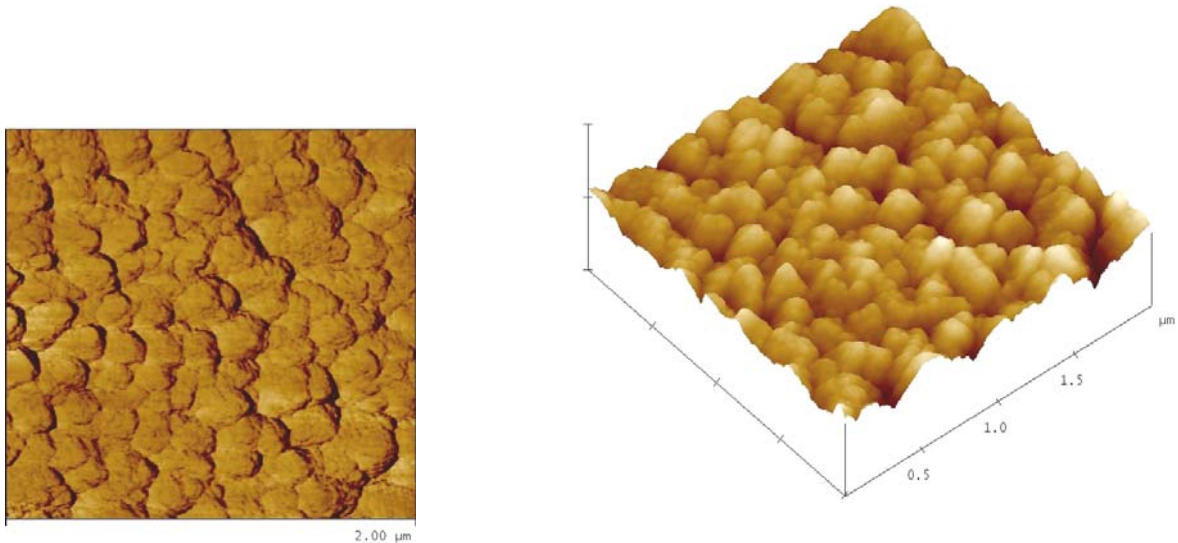

Figure 3.4: 2D and 3D AFM image of a TiC film deposited by spray pyrolysis without the laser heating.
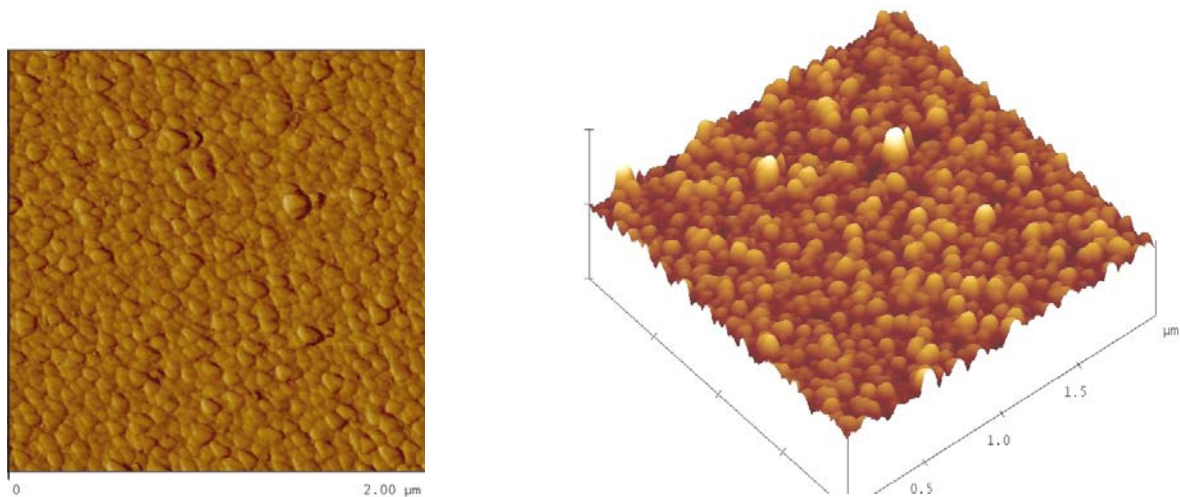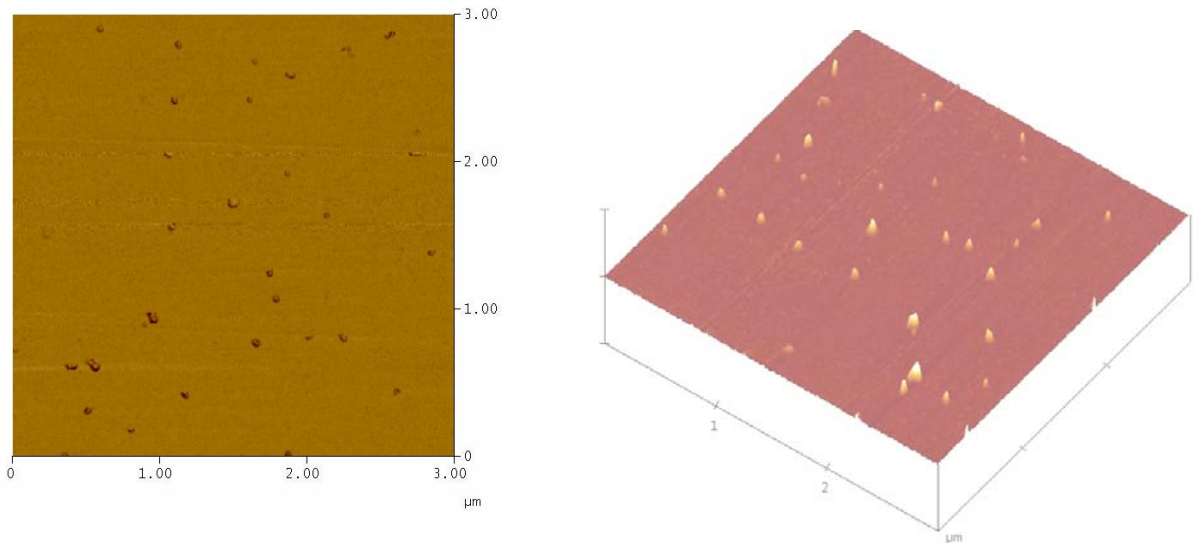
Figure 3.5: 2D and 3D AFM image of a TiC film deposited by spray pyrolysis with the laser heating.

In fig 3.4 and 3.5, one can clearly see that in the presence of laser heating the grain sizes are much smaller than in absence of laser heating. Without laser heating the average size of the grains is about 150nm in radius, while with laser heating, the grain size is reduced to about 50nm in radius. The reason for the change in particles size, with and without a laser, can be explained in terms of evaporation of the solvent. As a droplet comes out of the nozzle, the laser heating of SF_6 results in the evaporation of toluene from the droplet. Then the droplet becomes denser as compared to the base composition, which is used in the precursor. The high density and smaller size reduce the possibility of droplet flattening when colliding with the substrate. This causes the deposited film to be consisting of well-defined particles as shows in the figure 3.5.

3.3 PARTICLE SIZE ANALYSIS

With decreasing concentration of the precursor the percentage of the compound present in a 1.5 μm droplet also decreases. Since laser heating evaporates the solvent, the solid particle produced will become smaller with decreasing concentration. The films deposited with precursor concentrations of 0.05M, 0.1M, 0.2M, and 0.25M have been analyzed by AFM to study the concentration-particle size relation in the spray pyrolysis process. Toluene was used as the solvent for all solution.

To investigate the initial growth of the particles precursor droplets were deposited for 30 second on silicon substrate. The substrate was heated to 400 ^{0}C. AFM images of individual particles formed at the early stage of growth with laser heating are shown in Fig 3.6. The AFM images show the initial particle sizes to be of about 50-60 nm.
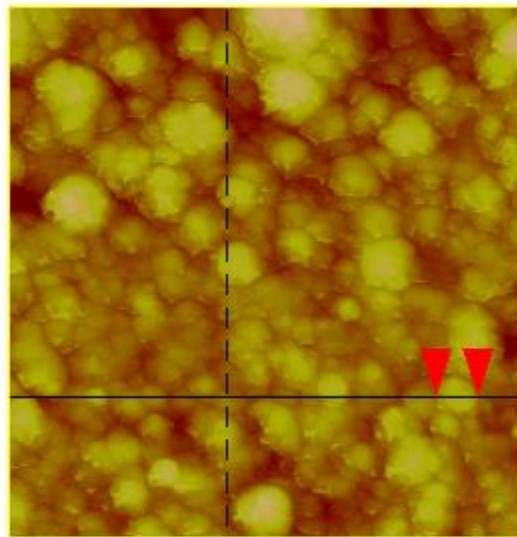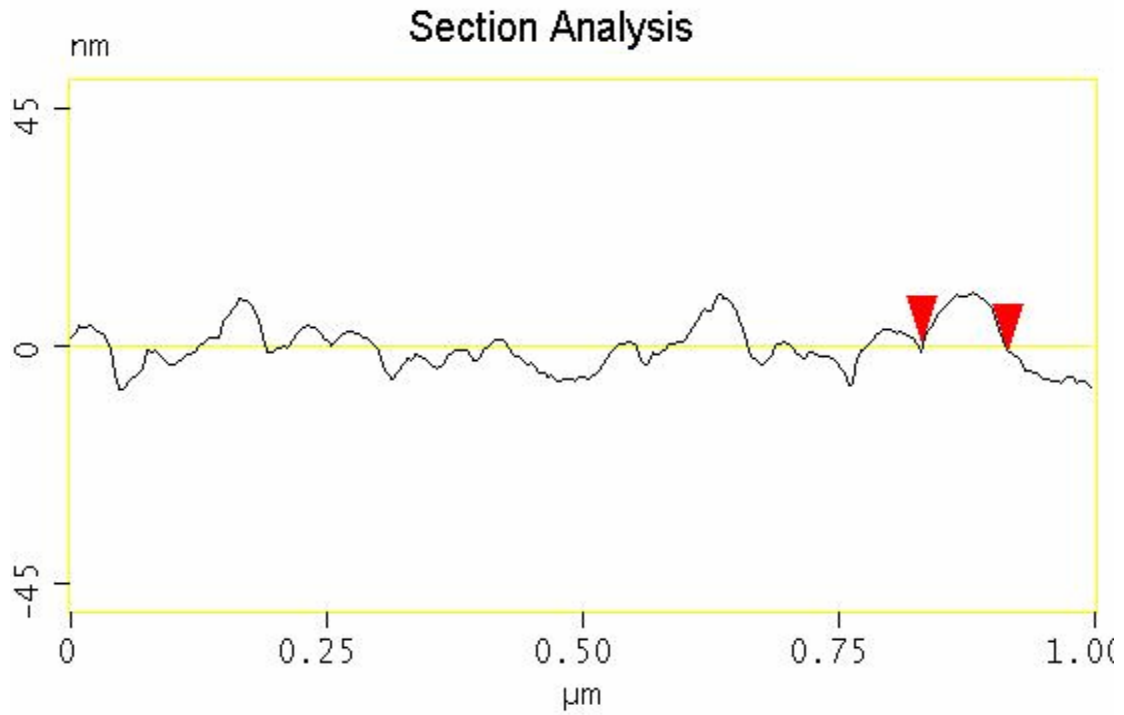

(a)
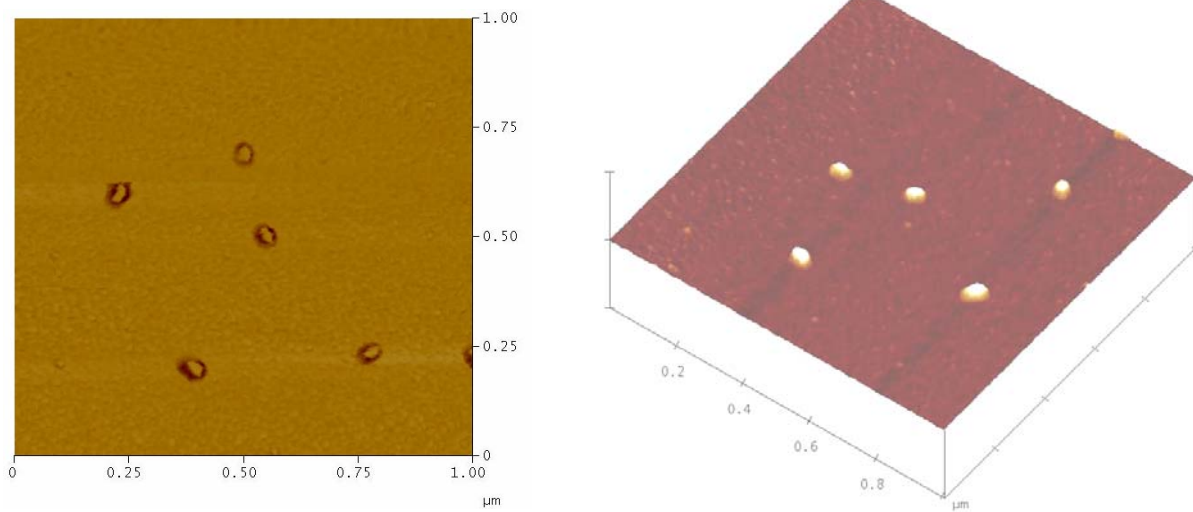
(b)

Figure 3.6: (a) 2D and 3D AFM image of a Fe_3O_4 film deposited by spray pyrolysis with the laser heating (1minute deposition). (b) Enlargement of figure (a).

The boiling point of toluene is 93 ^{0}C. Therefore, if the laser heating is sufficient to heat the carrier gas SF_6 above this temperature, complete evaporation of the solvent can be expected.

Section Analysis

L	82.031 nm
RMS	3.378 nm
lc	DC
Ra(lc)	2.695 nm
Rmax	10.436 nm
Rz	10.347 nm
Rz Cnt	2
Radius	85.977 nm
Sigma	0.560 nm

Figure 3.7: 2D AFM image of a Fe_3O_4 (0.25M Fe $(CO)_5$,substrate Temp 400 ^{0}C) film deposited by spray pyrolysis with the laser heating.

27

Section Analysis
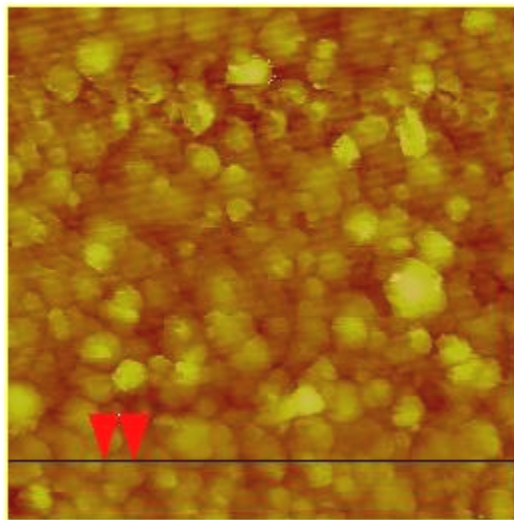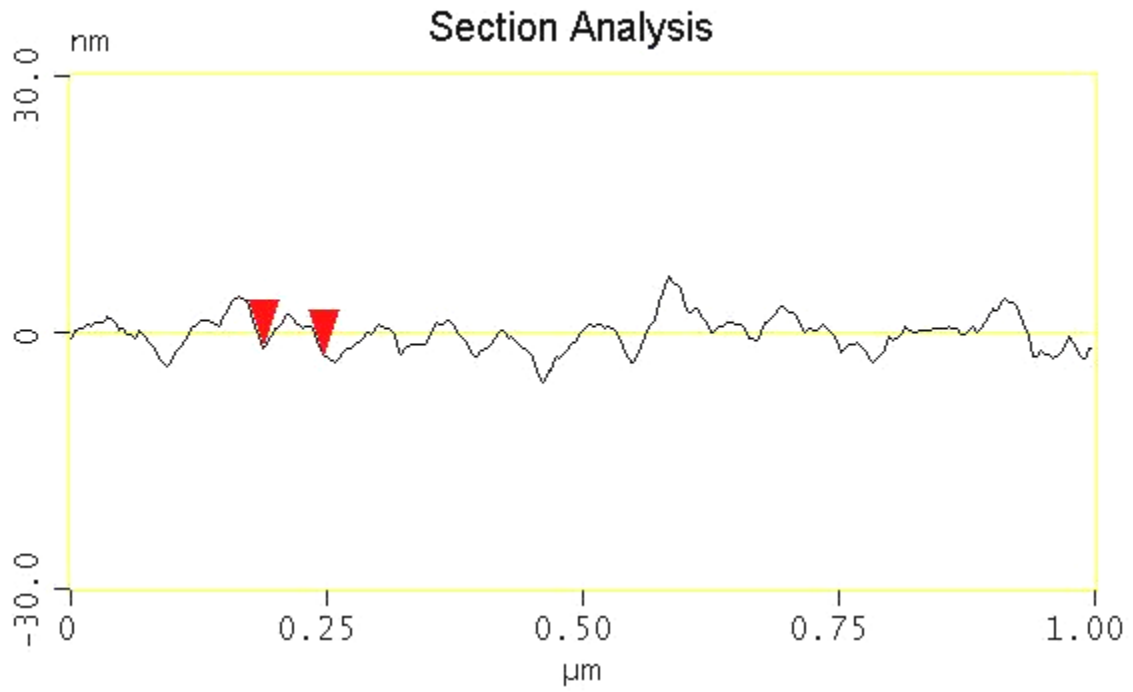
L	58.594 nm
RMS	1.370 nm
lc	2.000 µm
Ra(lc)	0.496 nm
Rmax	4.484 nm
Rz	4.430 nm
Rz Cnt	2
Radius	104.10 nm
Sigma	0.390 nm

Figure 3.8: 2D AFM image of a Fe_3O_4 (0.2M Fe $(CO)_5$, substrate Temp 400 ^0C) film
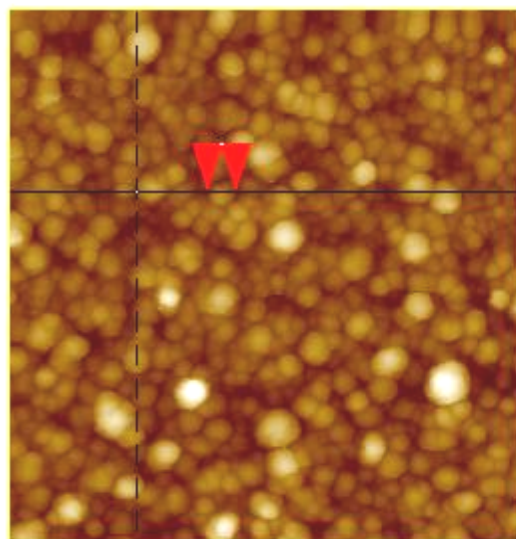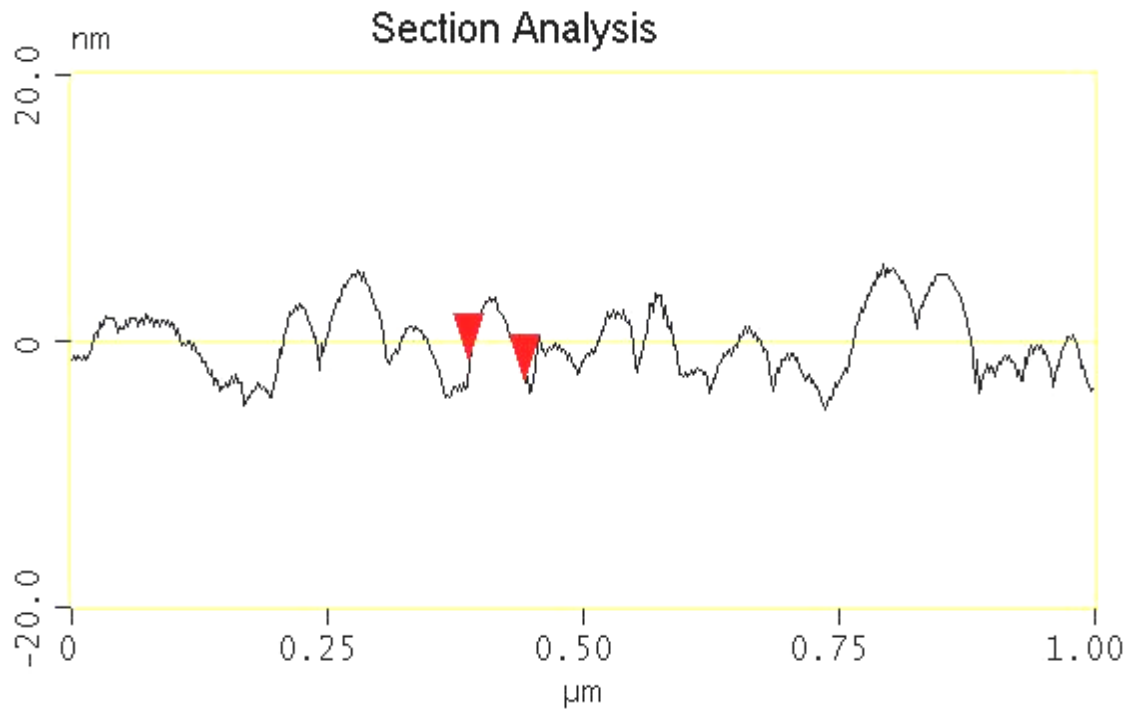
deposited by spray pyrolysis with the laser heating

Figure 3.9: 2D AFM image of a Fe_3O_4 (0.1M Fe $(CO)_5$, substrate Temp 400 ^{0}C) film deposited by spray pyrolysis with the laser heating

Figure 3.10: 2D AFM image of a Fe_3O_4 (0.05M Fe $(CO)_5$, substrate Temp 400 ^{0}C) film deposited by spray pyrolysis with the laser heating
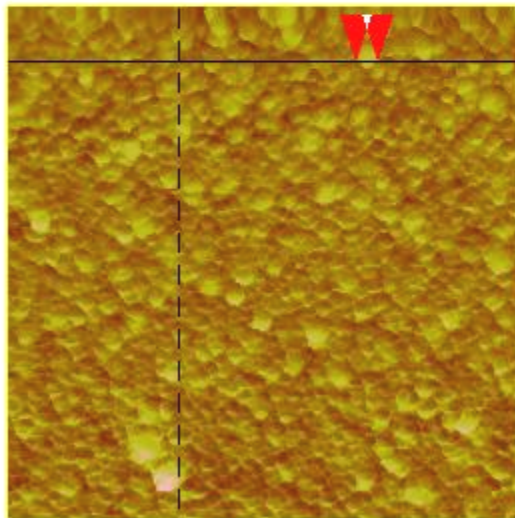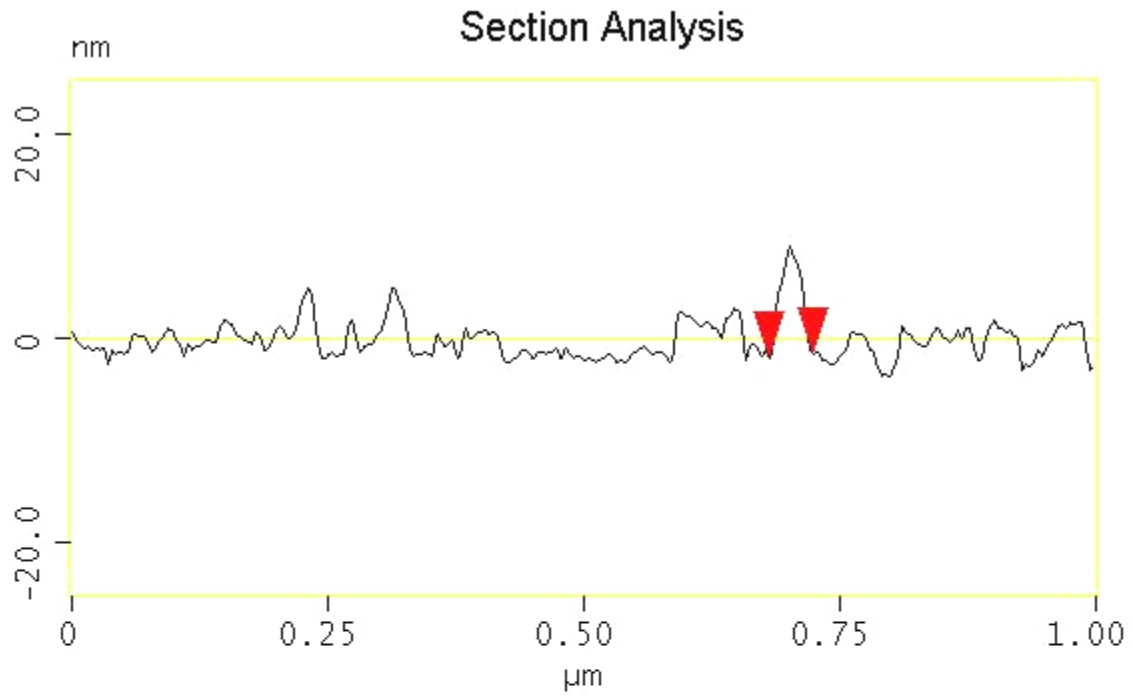
The above figures (from fig 3.7 to 3.10) show the cross sectional AFM analysis of samples with different concentrations. They show the cross sectional diameter of grains in each samples, which represent the mean diameters of their particle distributions. To select the mean particle from the distribution, a statistical method was used as follows;

This method is based on collecting random particles (about 50 or more) from each sample. To determine this change, a statistical study was conducted on each sample. First, the diameter measurements of 50 randomly selected particles in each particle distribution were recorded followed by the construction of a histogram of number of particles counted verses diameter for each sample. The results were fitted into a standard Gussian distribution to determine the mean value. Particle distribution for films deposited with the concentration of 0.25M, 0.2M, 0.1M and 0.05M are shown in Fig 3.11, 3.12, 3.13 and 3.14.

The chart contains a legend box with the following text:

Data: Data1_B
Model: Gauss

Chi^2/DoF = 12.26106
R^2 = 0.89415

y0	1.92455	±1.52302
xc	80.75192	±1.72017
w	25.25392	±4.10478
A	769.05508	±136.71038

—— Gauss fit of Data1_B

Axis labels: percentage (%) out of 50 (y-axis), particle size (nm) (x-axis)

Figure 3.11: Percentage of particle diameters counted for each set of 10nm blocks when concentration is 0.25M.
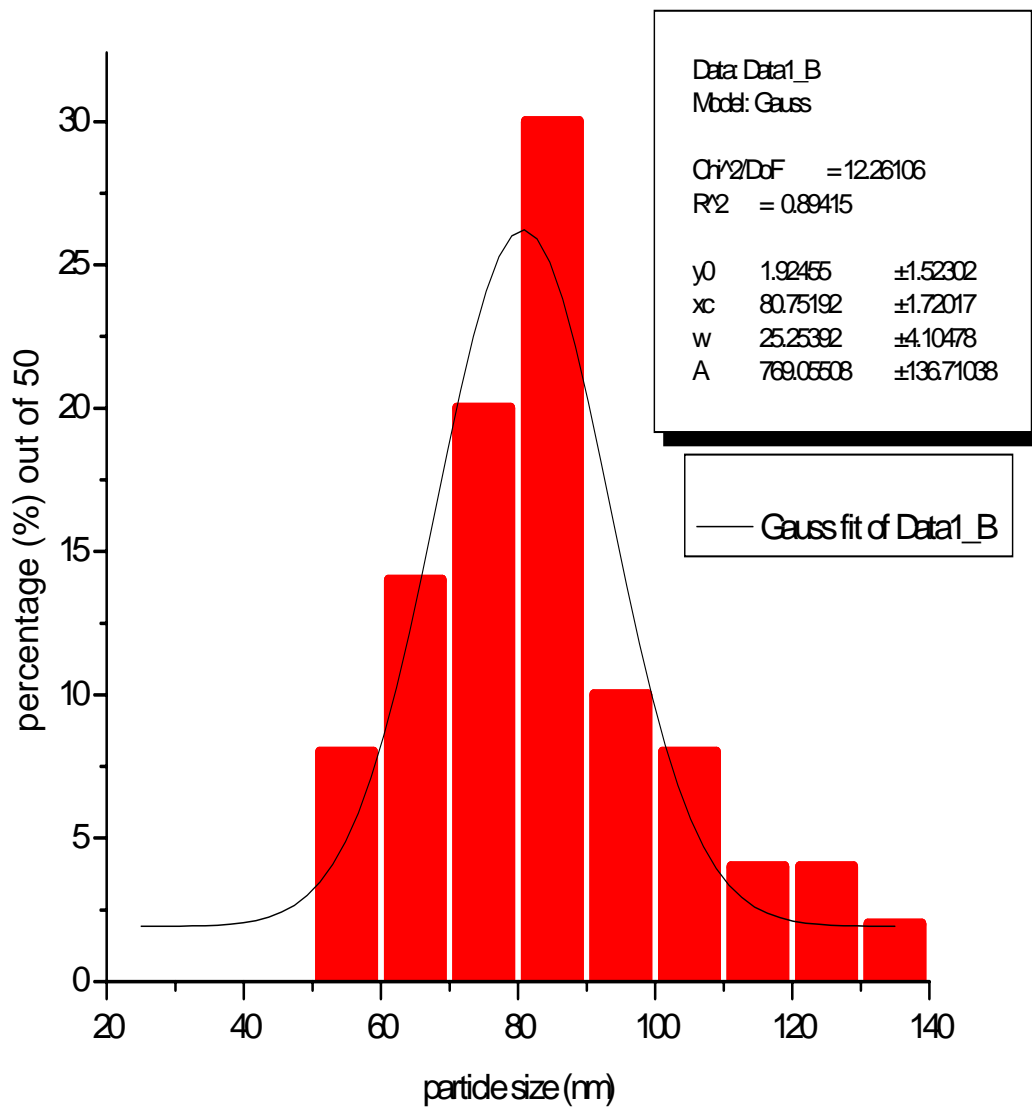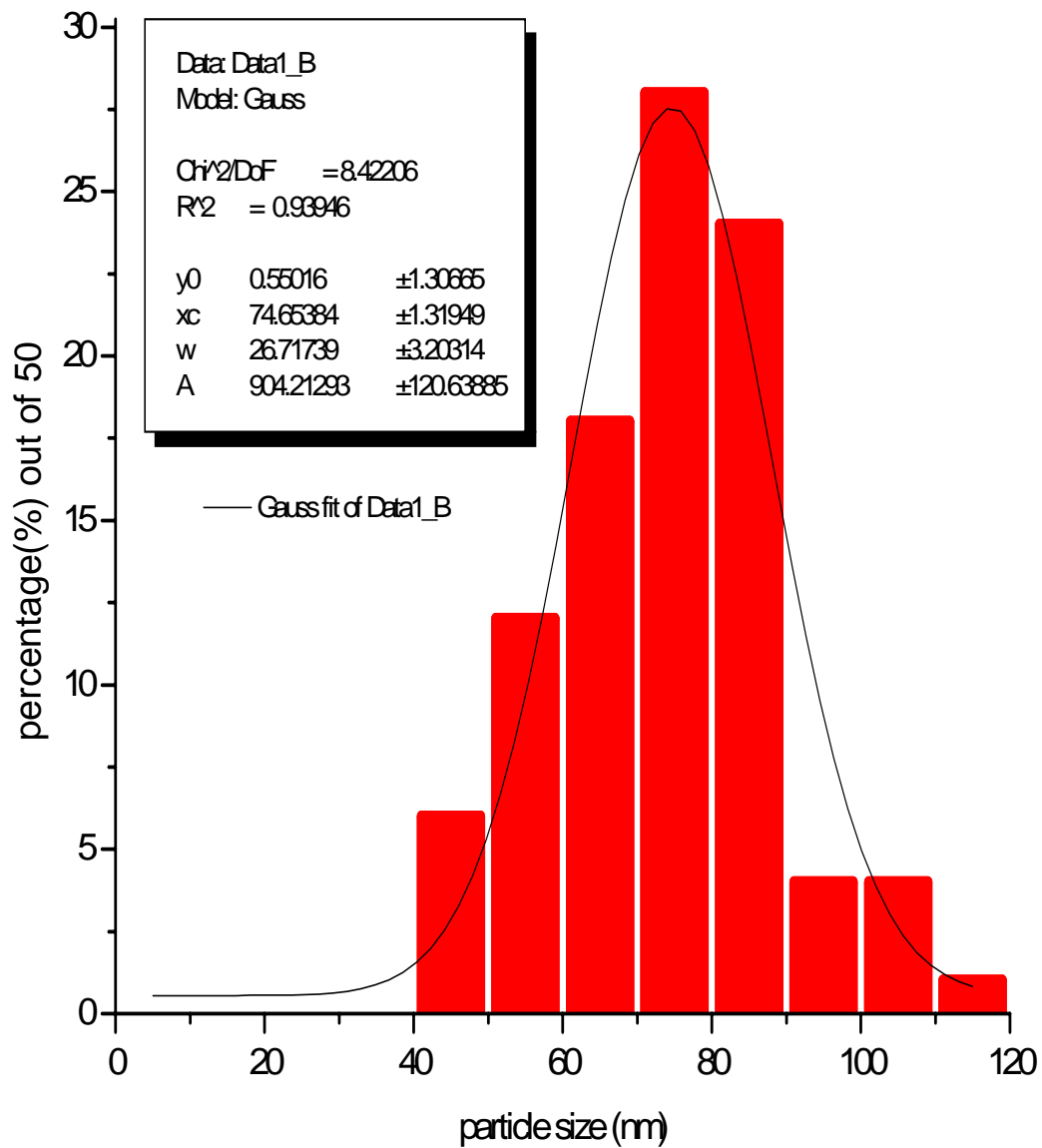
Figure 3.12: Percentage of particle diameters counted for each set of 10nm blocks when concentration is 0.20M.
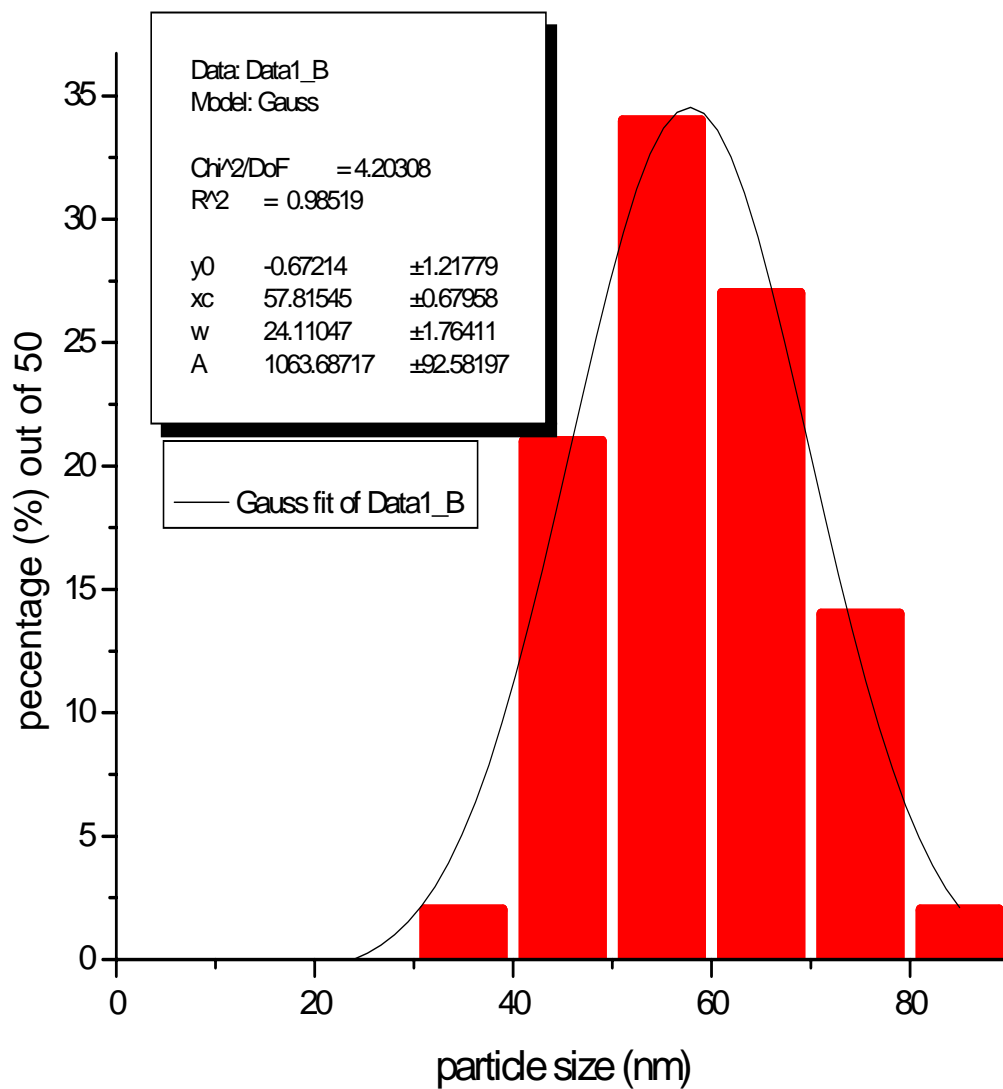
Figure 3.13: Percentage of particle diameters counted for each set of 10nm blocks when concentration is 0.10M.
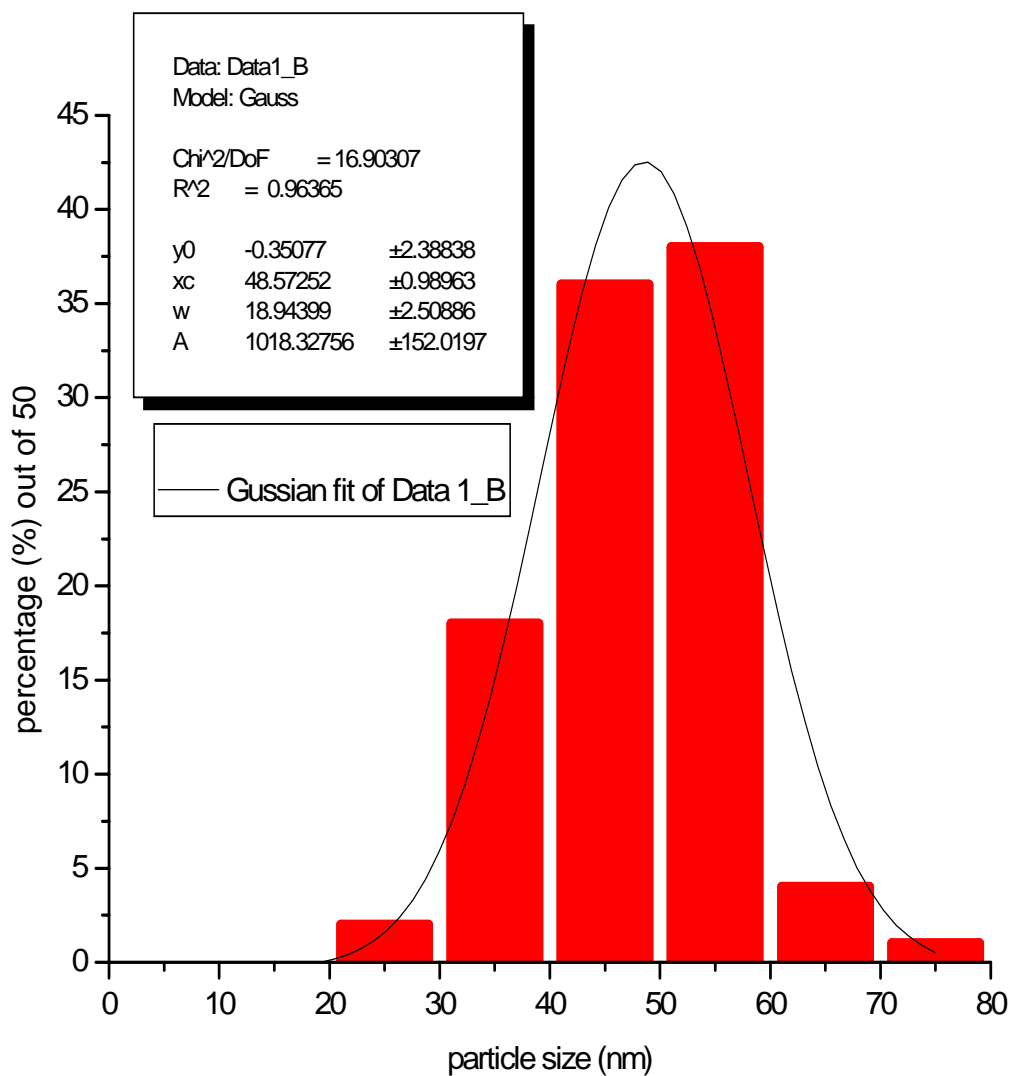
Figure 3.14: Percentage of particle diameters counted for each set of 10nm blocks when concentration is 0.05M.
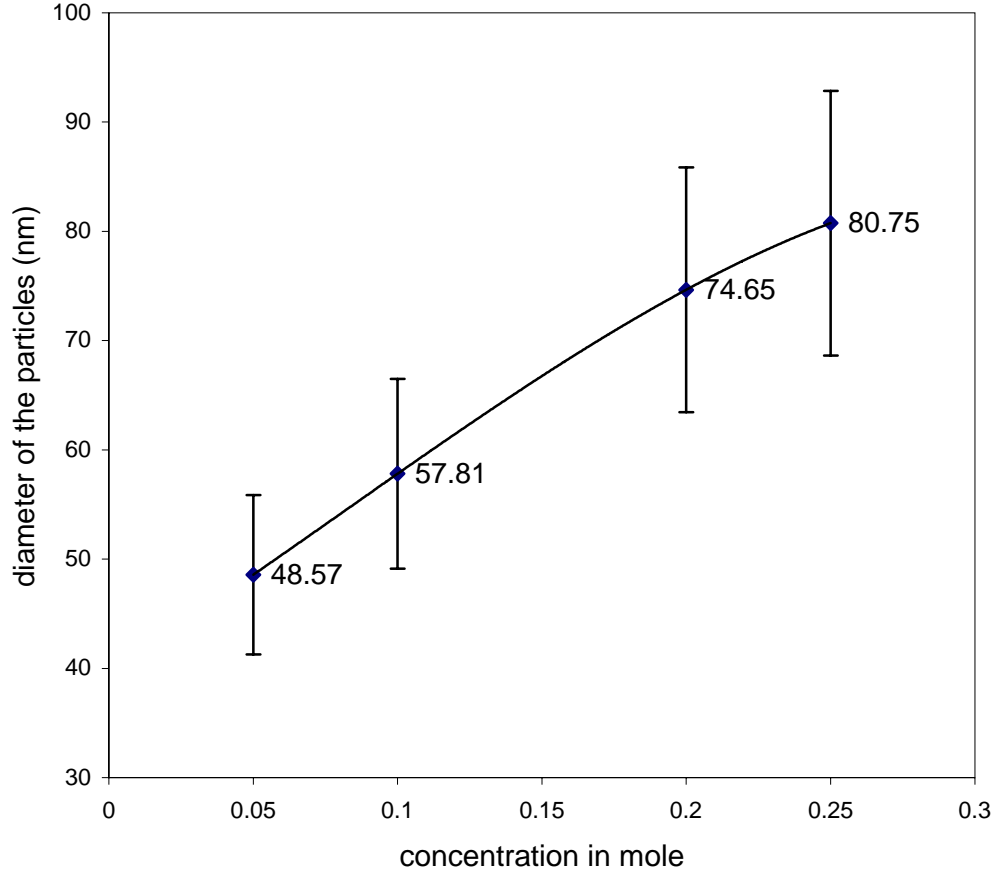
Figure 3.15: Particle size dependence on the concentration of the precursor.

The graph above shows the particle size variation with the concentration for the sample. According to the graph, it is clear that the size of the particles have been decreasing with the concentration. Also this variation can be perfectly fitted with a 3rd order polynomial ($f(x) = -1000x^3 + 240.67x^2 + 166.2x + 39.783$).

The AFM analysis of the different samples shows a clear change in grain size in different concentrations. A simple model can be used to compute the expected particle size for a given concentration. In this analysis, it is assumed that the droplet is 1.5 μm in

diameter and the solvent is completely evaporated from the droplet by laser heating

before it arrives at the substrate. Also the drop remains a spherical particle on the

substrate after the collision. The model is outlined below.

The case where the concentration is 0.05M, the number of Fe $(CO)_5$ molecules in

a 1.5µm droplet of Fe $(CO)_5$ (formula weight 231.4) in toluene are;

$$concentration \times 10^3 \times 6.023 \times 10^{23} \times \frac{4\pi}{3} \times (0.75 \times 10^{-6})^3$$

$$= 5.32 \times 10^7$$

Since 3 molecules of Fe $(CO)_5$ lead to a Fe_3O_4 molecule after dissociation, the

number of Fe_3O_4 molecules in a 1.5µm droplet are;

$$= \frac{5.32 \times 10^7}{3} = 1.77 \times 10^7$$

Assuming the final product to be a solid spherical particle of Fe_3O_4 with a density

of 5.7 g/cm3 (bulk density of Fe_3O_4), the size of the Fe_3O_4 particle produced by a droplet

can then be calculated as follows. (Since V= M /ρ)

37

$$V = \ concentration \times 10^3 \times \frac{6.023 \times 10^{23}}{3} \times \frac{4\pi}{3} \times (0.75 \times 10^{-6})^3 \times \frac{231.4 \times 1.66 \times 10^{-27}}{5700(density)}$$

$$\text{Since} \quad \frac{M}{p} = V = \frac{4\pi\left(\frac{d}{2}\right)^3}{3}$$

$$d(size) = 35.747 \times 10^{-3} \times (concentration)^{\frac{1}{3}}$$

$$d(size) = cons\,tant \times (concentration)^{\frac{1}{3}}$$

$$y = mx^{\frac{1}{3}} (type\_relation)$$

Table 3.1, shows the computed average particle size for concentrations used in the experiment

Concentration (M)	Size of the particle (nm)
0.05	131.69
0.1	165.92
0.15	189.93
0.2	209.05
0.25	225.52

Table 3.1 the computed average particle size for different concentration.
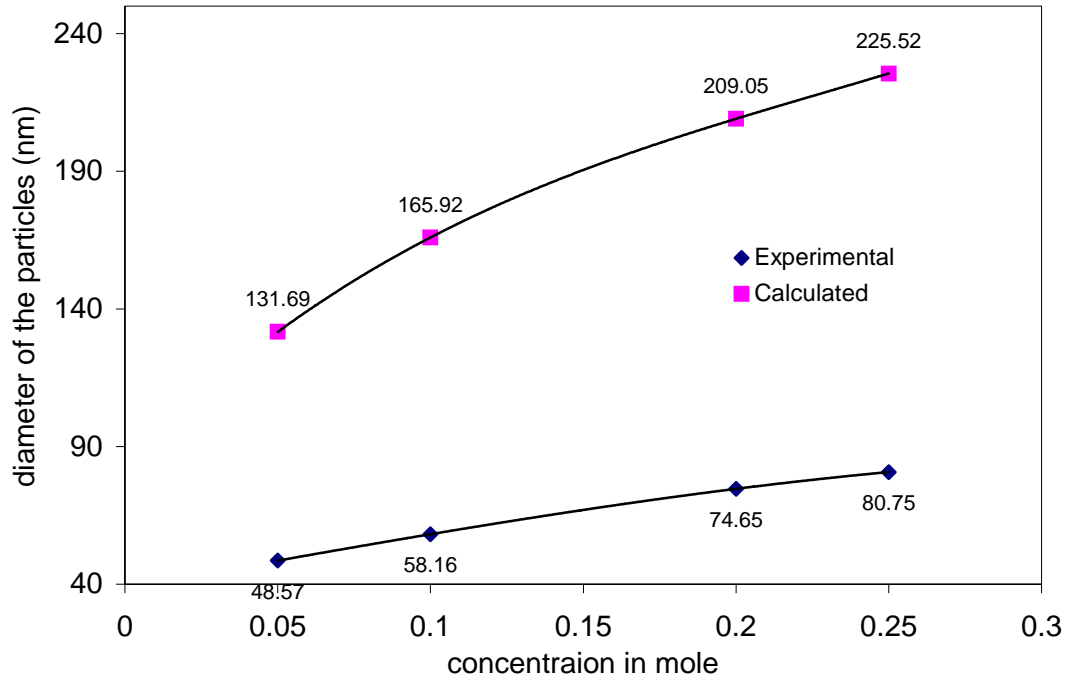
Figure 3.16 Comparison of the computed & experimental diameter of the grain sizes with changing concentration.

The computed grain sizes of each concentration along with the experimental data are shown in graph 3.16. It is clear that there is a considarable difference between the calculated and the experimental graphs. The calculated values became more than twice as the experimental values. This difference can occur due to several reasons.

The first reason is, the concentration of the solution that was considered in the calculation is much higher than the concentration of prepared precursor. This is because the organomatallic precursor, Pentacarbonyliron, is in liquid form and is highly light sensitive. Exposure to light and air causes iron pentacarbonyl to gradually decompose.

This leads to a reduction in concentration with time. For example, the actual molar ratio of 0.05M solution could be much lower.

The second reason is, in the calculation we assumed that only the solvent in the droplet is evaporated. In addition to the solvent the precursor will also evaporate in the hot SF_6 gas, when the drop travels through the laser spot. If the drop falls on the heated substrate without complete decomposition, further evaporation will make the final particle size much smaller than the computed valve.

Therefore, the number of atoms available in the real situation can be lot less than the calculated amount. The actual concentration also can be lot less than in the calculation.

CHAPTER 4

ANALYSIS OF GROWTH PARAMETERS

As we discussed in the previous chapter, the formation of the film mainly depends on how much energy is absorbed by the droplet as it passes through the laser beam. There is an optimum condition to maximize the energy absorbed to the droplet. One of the parameters that determine the maximum energy coupling is the flow rate of the carrier gas. The flow rate determines how much time the droplets are kept in hot region while it passes through the laser. When the droplet interacts with the hot gas for an extended time, the temperature of the droplet reaches to a higher value and causes solvent evaporation. The optimum condition of the process can be found by studying the energy absorption to the carrier gas and temperature variation of the carrier gas in different flow rates of carrier gas.

4.1 EFFECT OF FLOW RATE ON LASER HEATING

The experimental arrangement shown in Fig 4.1 was used to study the effect of the flow rate on laser heating of the carrier gas SF_6.
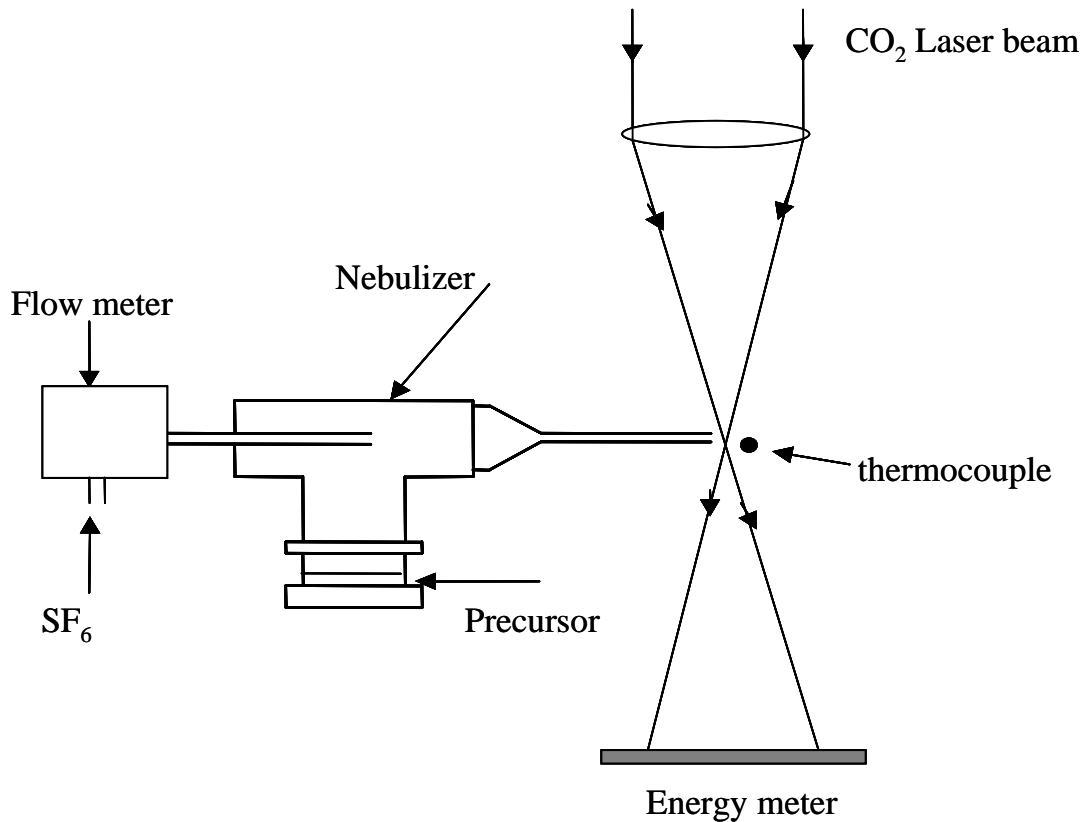
Figure 4.1 Experimental set-up for study of flow rate effect on Laser heating

The temperature of the Laser heated gas was measured by a K-type thermocouple placed in front of the nozzle opening just after the laser focus. The laser energy absorbed to the flow was measured by placing a energy meter on the Laser path, outside the chamber as shown in fig 4.1.The graph 4.2 and 4.3 respectively, show the variation of the temperature of the flow jet (spray) and the variation of the laser energy with respect to the flow rate.
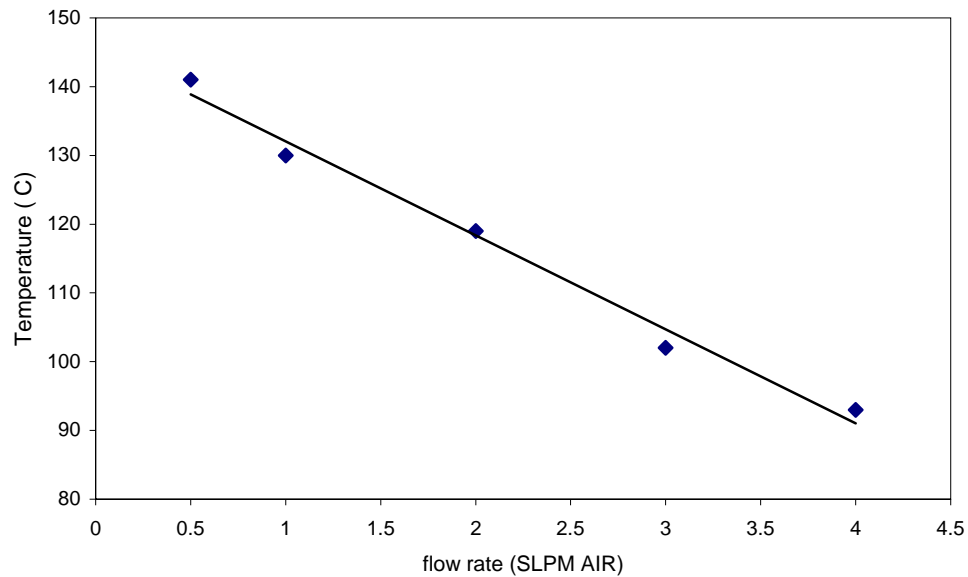
Figure.4.2: Graph of Temperature of flow verses Flow rate of SF_6 gas.

The results obtained in figure 4.1 show that the temperature is linearly decreasing with increasing of the flow rate of the carrier gas. This can happen due to two reasons.

When the flow rate increases, the droplet has less time in contact with the laser. Therefore, it absorbs less energy from the laser beam and causes the temperature to drop.

The second reason is, as the flow rate is increased, the concentration of SF_6 molecule in the chamber also increases. Then the pumping is not enough to take all the SF_6 molecules coming into the chamber. Therefore, SF_6 molecules in the chamber absorb some amount of laser energy before the laser interacts with the flow out of the nozzle. This effect leads to a drop in temperature of the flow.
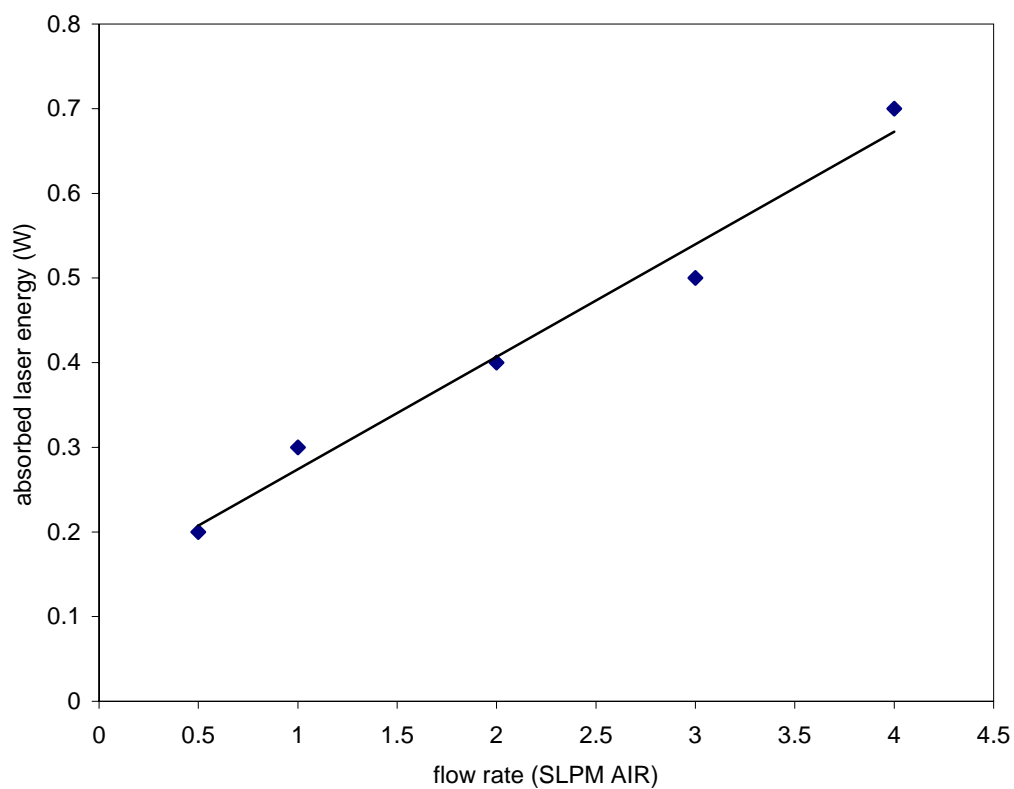
Figure 4.3: Graph of absorbed laser energy verses flow rate of the droplets.

The results in figure 4.2 show that the absorption of laser energy is linearly increasing with the increasing of flow rate. The reason for this is, as the flow rate increases, the number of SF_6 passing through per second increases, giving rise to an increase in the amount of energy absorbed.
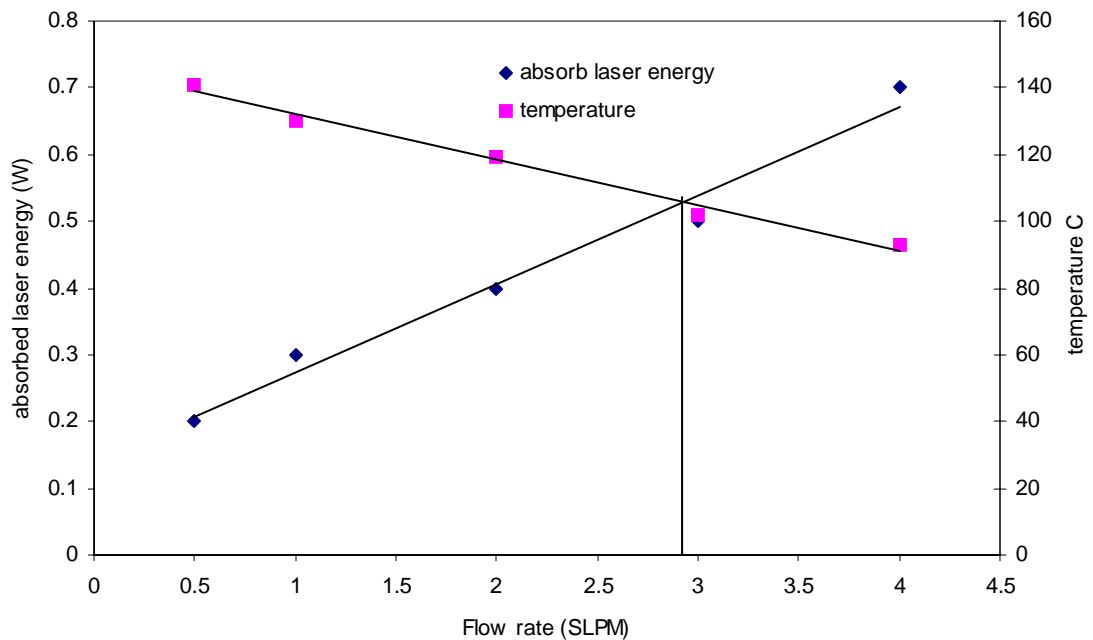
 Figure 4.4: Normalize graph of temperature verses flow rate and laser energy verses flow

rate.

The figure 4.4 represents the normalized graphs of temperature versus flow rate

on one scale and absorbed laser energy versus flow rate in the other scale. As can be see

in the figure, the point where two graphs intercept is identified as the optimum point of

operation for the experiment. Since the flow rate is the only varying parameter, the flow

rate of the carrier gas has to be fixed at the optimum value, which is 3.0 SLPM AIR.

(This Flow rate value depends on the setup. It can be adjusted depending on any changes

in the set up such as size of the nozzle and pressure of the chamber).
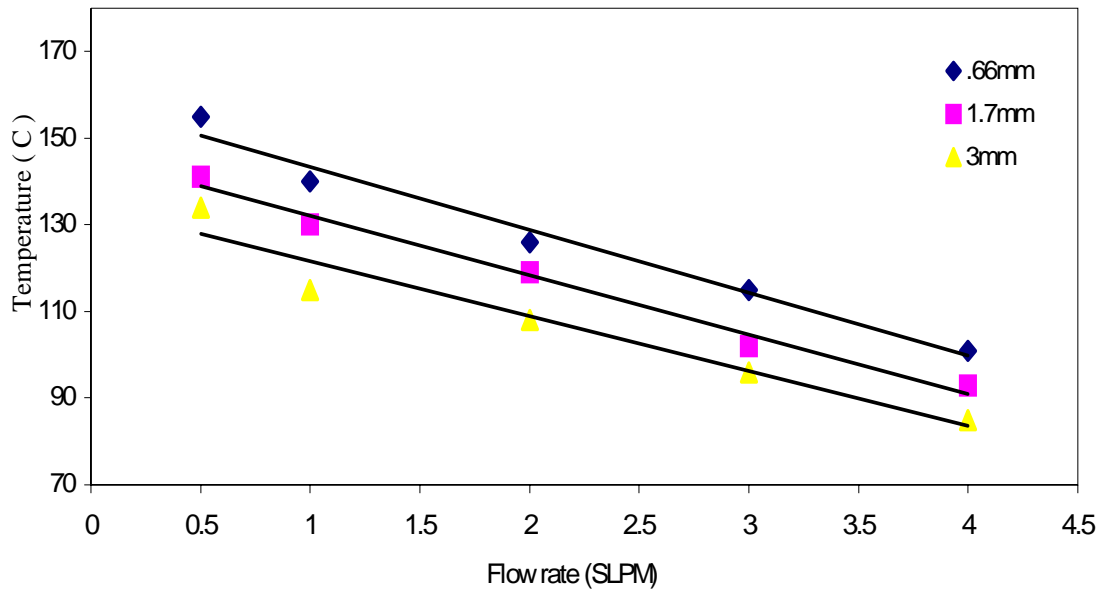
Figure 4.5: Change in temperature of the flow with diameter of the nozzle.

The above graph shows the temperature variation with respect to flow rates for different nozzle diameter. As shown in the figure, when the diameter of the nozzle decreases, the temperature of the flow rate is shifted towards a higher elevation by keeping the gradient almost the same. Therefore the nozzle size and the focusing of the beam are critical factors to transfer a maximum amount of energy from the laser to the flow. To obtain the maximum amount of energy these factors have to be optimized. It can be done using the beam optics.

4.2 THERMAL MODEL FOR LASER ASSISTED SPRAY PYROLYSIS

As a principle, in beam optics, the beam waist radius is important for maximum energy (power). It is directly related to the intensity of the beam. Within any transverse plane, the beam intensity assumes its peak value on the beam axis, and drops by the factor $1/e^2 \cong 0.135$ at the radial distance W (z). Since 86% of power (energy) is carried within a circle of radius W (z), we regard W (z) as the beam radius (also called the beam width). It assumes its minimum value W_o in the plane z=0, called the beam waist. Thus W_o is the waist radius. The waist diameter 2W is called spot size. To absorb maximum amount of energy from the laser beam, the nozzle size has to be the same as the spot size. Since our nozzle size is fixed the only way this is achievable is by changing the position of the lens so as to match the nozzle size.

In our application, for a given λ(wavelength of CO_2 laser), the spot size can be found by using following relation. (λ= 10.6 for CO_2, W_o =10mm, f = 80mm).

$$2W = \underline{4} \; \lambda. \; \underline{f}$$
$$\pi \quad 2Wo$$

For a CO_2 laser, according to the above formula the minimum spot size is found to be 0.27mm.
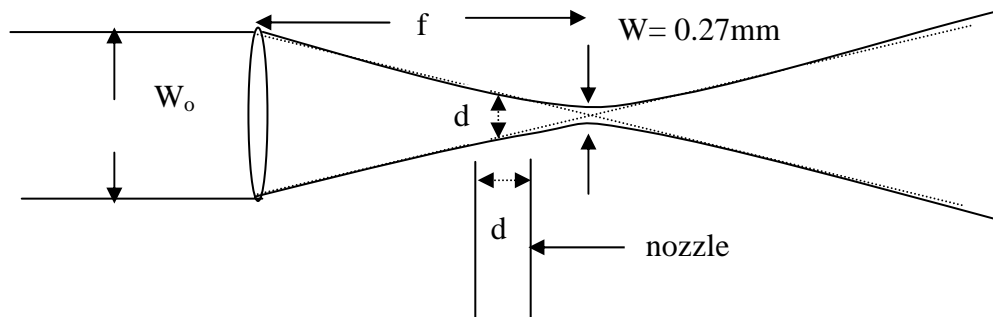

Figure 4.6 Focusing a collimated beam to match with the size of the nozzle diameter.

The position of the lens is selected so as to have the required spot size to match the diameter of the nozzle.

The experiment was run by keeping the set up under the configuration shown in fig 4.6. The flow rate versus temperature data for that configuration is shown in fig 4.7. The calculated data is also shown in the same figure. To calculate this data, we used the following mathematical model for this computation. We assumed the cross-section of the beam to be a top-hat profile that has a beam width of W, equal to the FWHM of the gaussian profile. We assumed this rectangular beam to be interacting with a gas volume of $W \times W \times d$, where d is the diameter of the orifice of the tube. R is flow the rate measured.
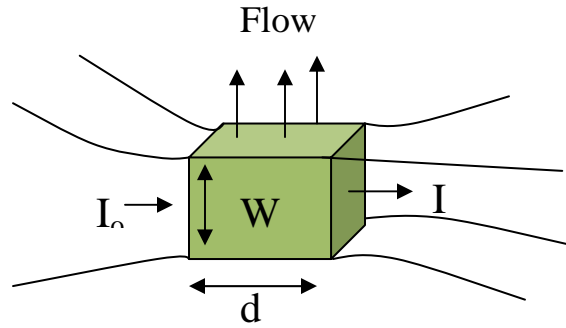
Intensity change within the absorbing volume $\Delta I = Io\,(\,1\text{-}e^{-\alpha d})$

ν =velocity of the flow

$$Q = m \times C \times \Delta T$$

$$I_o(1 - e^{-\alpha d}) \times W \times t = W^2 \times d \times \rho \times C \times \Delta T$$

$$But \ \ t = \frac{W}{v} = \frac{Wd^2}{R}$$

$$P(1 - e^{-\alpha d})\frac{Wd^2}{R} = W^2 d \times \rho \times C \times \Delta T$$

$$\Delta T = \frac{P \times d}{\rho \times R \times C \times W}(1 - e^{-\alpha d})$$

Here, $\rho = 6.164 \ kg/m^3$, $C = 598.8 \ J/Kg.K$, $P = 3W$, $\alpha = 0.7cm^{-1}$

$A_1V_1 = \text{flow} \times 0.16 \times 10^{-4}$, $W=0.5mm$.

Flow rate (SLPM)	Actual Flow Rate (SLMP)	Temp (C)
0.5	0.12	189.64
1.0	0.24	108.32
2.0	0.48	67.66
3.0	0.72	54.01
4.0	0.96	47.33

Table 4.1 Theoretical change of temperature with flow rate in perpendicular
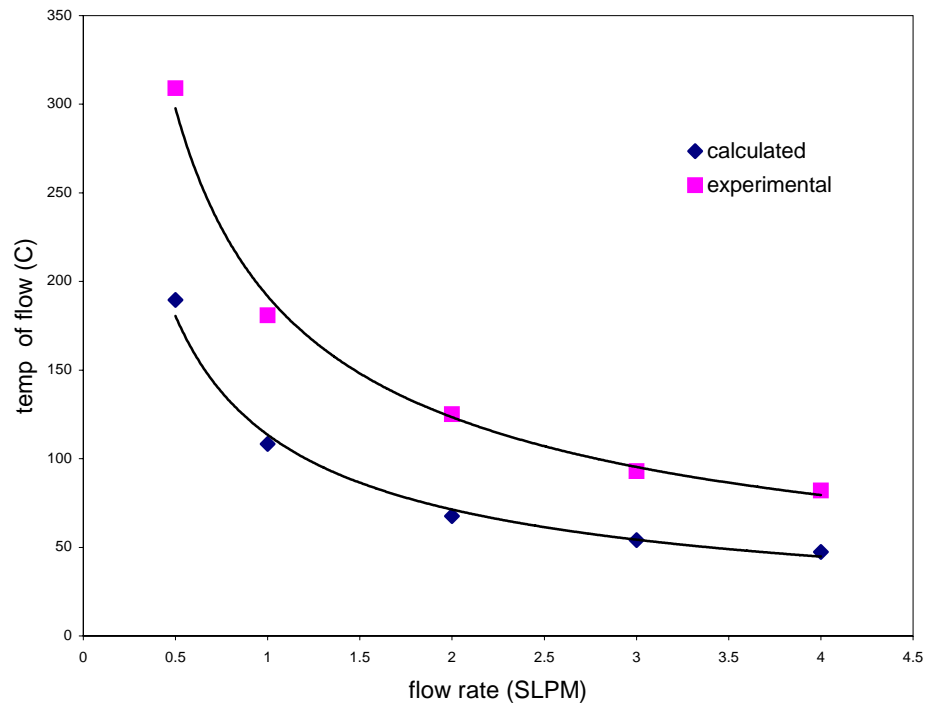
configuration.

Figure 4.7 Graph of Temperature of flow verses Flow rate of the droplets when the

nozzle is set out of the chamber perpendicular to the flow.

The main drawback for this configuration is when the flow rate is at 3.0 (where is

the optimum rate for the experiment) the temperature of the flow does not reach the

decomposition temperature of the chemical. The reason is, the time available for flow to

interact with the laser is limited in this configuration. One can increase the laser-gas

interaction time by setting the laser parallel to the flow path. In this configuration the

laser energy is absorbed by SF_6 for a longer time period, and therefore, expect the final

temperature of the gas to be much higher.

4.2.1 ON-AXIS LASER HEATING

The experimental arrangement for on axis laser heating is shown in fig 4.8

Figure 4.8 experimental arrangements for parallel configuration.

The Laser beam was focused to the nozzle opening so that the laser would not hit the glass wall. A nitrogen jet was introduced to change the direction of the flow so that the particles were steered away from the path of the laser.

This experiment was run to see the temperature variation of the flow when the system is outside the chamber. By doing this, one can avoid the absorption that takes place inside the chamber due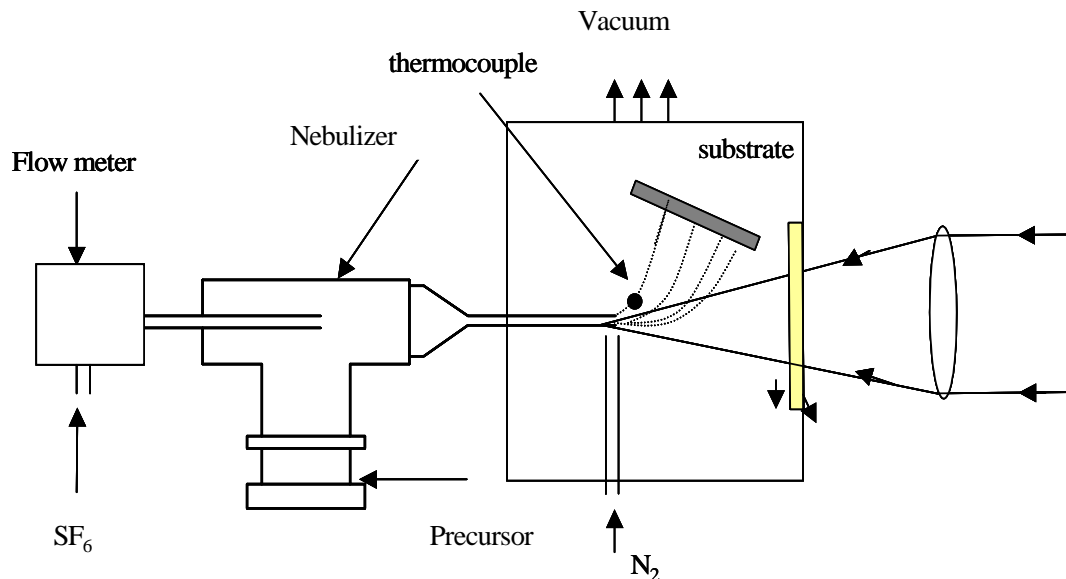 to the surrounding SF_6 gas. The graph in fig 4.10 shows the temperature variation for different flow rates. Fig 4.10 also includes a computed temperature variation with flow rate using a thermal model (fig 4.9).

The fig 4.8 shows the situation where the laser beam is directed parallel to the flow. By making the laser beam parallel to the flow, the molecules in the flow can be exposed for a longer length of time to the laser energy. As a result of this, the temperature of the flow went up compared to the perpendicular configuration. The drop in temperature as the flow rate increases is expected in both situations. At high flow rates the laser-gas interaction time is reduced and the volume of the gas heated per second is increased.

Fig 4.9 shows the data for a mathematical model for the configuration where the laser beam is parallel to the flow. The temperature in this graph for each flow rate was found by integrating a dx cross section at x distance through out the path of the particle in a beam to the edge of the nozzle.

51
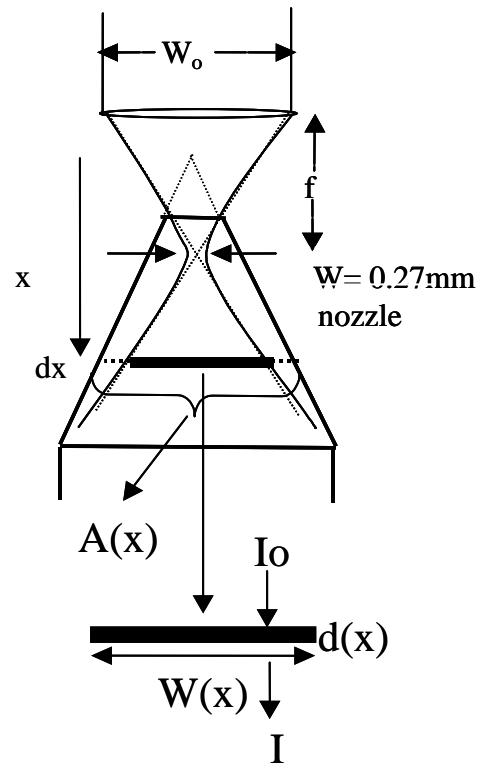
Figure 4.9 Parallel configuration of the nozzle

The change in intensity across an absorbing laser of thickness dx is given by

$$\Delta I = I_0 e^{-\alpha d} dx$$

Since this energy is absorbe into a crossection of $\pi \dfrac{W^2(x)}{4}$

Power absorbed $= \Delta I \pi\ W^2(x)/4$ Watts

flow rate across $W(x) = \dfrac{A_1 V_1}{A(x)} \times \pi\ \dfrac{W^2(x)}{4}$

Here, A(x) is the crossection of the nozzle at a distance x

$$P \alpha e^{-\alpha d} dx = \dfrac{A_1 V_1}{A(x)} \times \pi\ \dfrac{W^2(x)}{4} \times D \times C \times \Delta T$$

Carrying out a thermal balance for the layer of thickness dx at a distance of x, an equation for the temperature can be obtained.

$$\frac{\alpha \cdot P \times 10^{-3}}{DCA_1V_1} \int \left(\frac{1}{.12\,x - 2.03}\right)^2 (.6x)^2 \exp\left(-\alpha \cdot x\right)dx = \Delta T$$

Here, $D = 6.164\ kg/m^3$, $C = 598.8\ J/Kg.K$, $P = 3W$, $\alpha = 0.7cm^{-1}$

$A_1V_1 = $ flow$\times 0.16 \times 10^{-4}$

Flow Rate (SLPM)	Actual Flow Rate (SLMP)	Temperature (C)
0.5	0.12	1476.8
1	0.24	756.9
2	0.48	389.4
3	0.72	268.6
4	0.96	208.2

Table 4.1 Theoretical change of temperature with flow rate in perpendicular configuration.
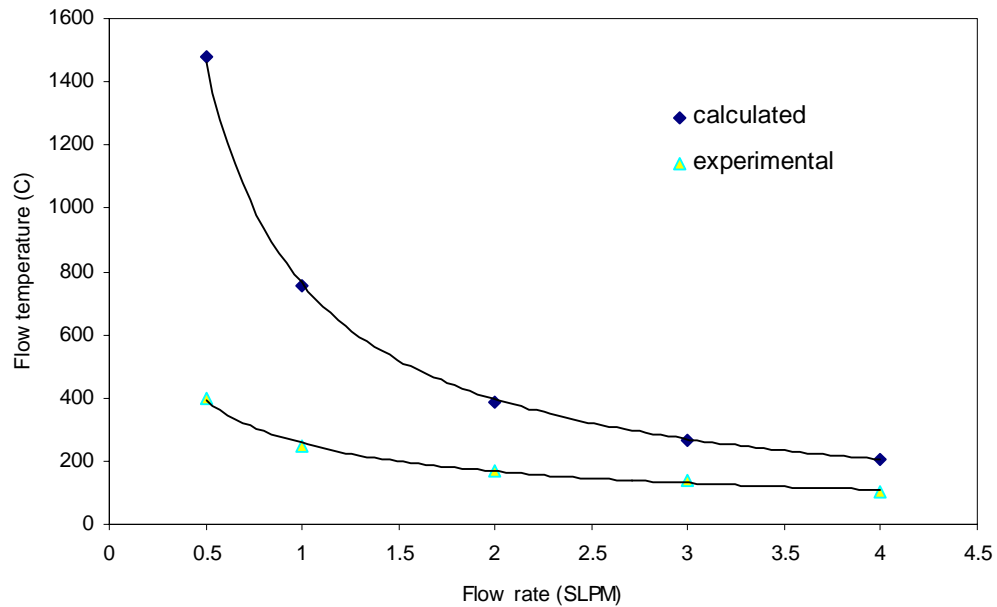
Figure 4.10 Graph of Temperature of flow Vs Flow rate of the droplets when the nozzle is set out of the chamber perpendicular to the flow.

Both experimentally measured and computed temperatures of the gas show a decrease with increase in flow rate. The measured values do not represent the exact temperature of the gas since the gas is significantly cooled by the N_2 gas jet when it comes in contact with the thermocouple.However, these measurements can be used to study the trend of temperature change with flow rate.

A film of iron oxide was deposited on a silicon substrate by using this on-axis heating configuration. The film is deposited only for about 5 minutes to study the initial growth.

The following AFM images are taken for the samples, which were made by keeping the nozzle parallel with the beam.

54

(a)

(b)

(c)

Fig 4.11 AFM images of the samples, which taken for parallel configuration. (a) Away from the center. (b) Enlargement of image (a). (c)Close to the center.

In this experiment the films are deposited in parallel configuration as in fig 4.8. Here, as shown in the schematic diagram, the flow coming out is heated by the laser,

deflected by the nitrogen flow, which is then collected on to the substrate. The center of the flow then deflects and is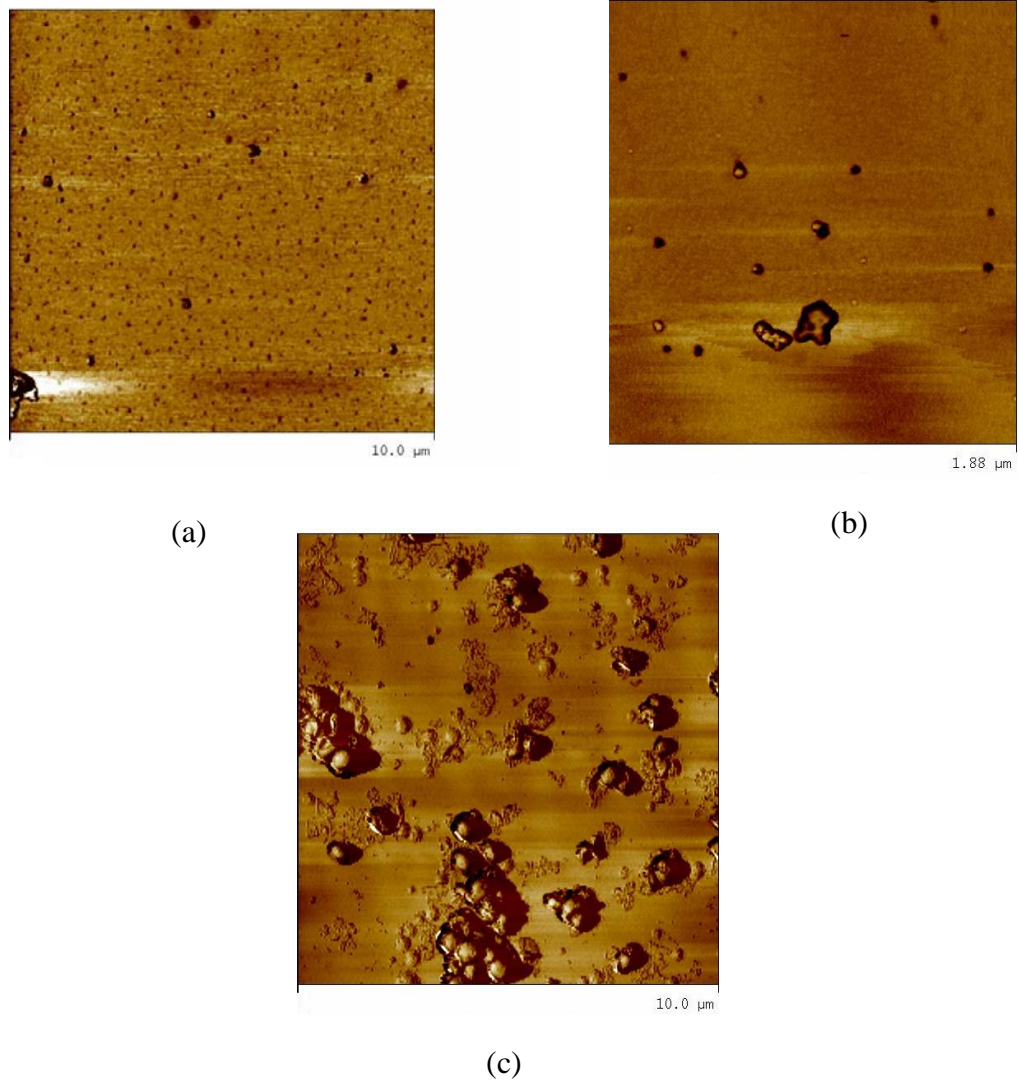 deposited on the center of the substrate (fig 4.11(c)), while "off axis" is deposited on the areas away from the center on the substrate (fig 4.11 (a)). While images (a) and (b) show nicely distributed isolated grains of about 50nm in diameter, image (c) shows large random grains of about 1000nm in diameter. The reason for this formation is mainly because of the variation of the temperature in the flow coming out of the nozzle. When laser is focused onto the flow, the intensity of the Gaussian beam drops by the factor $1/e^2$ as it goes away from the focused point. As a result, the temperature at the center reaches much higher values compared to off axis. The "on axis" temperature may be sufficient to melt the formed particle, causing them to agglomerate and form large particles as seen in fig 4.11(c). But on the other hand, comparatively low "off axis" temperature is sufficient to evaporate the solvent and decompose the precursor to form a solid particle, but is not sufficient to cause melting and agglomeration.

Therefore, it is obvious that the temperature for decomposition of the chemical can be reached in parallel configuration. In order to accomplish the complete decomposition one can set the system in such a way that it is decomposed completely as the chemical coming out. Therefore, the parallel configuration gives us a promising result in making thin nanocoatings.

CHAPTER 5

NANO GRAINED FILM GROWTH BY CHEMICAL SELF ASSEMBLY AND VAPOR PHASE GROWTH

5.1 BOTTOM-UP APPROACH FOR NANO-STRUCTURED FILM GROWTH

Nanostructured surfaces, films with morphological features in the nanometer range and ordered assemblies of nanometer-sized particles are interesting class of nanomaterials with great technological potential. Innovative applications for these new materials include high-density information storage media, biological sensor arrays, magnetic fluids, medical diagnostics and catalysts. Compared to conventional surface science techniques, such as gas-phase synthesis and nanostructuring or deposition of nanoparticles under ultrahigh-vacuum condition, the soft-matter approach is a scientifically and economically interesting alternative. In this approach self-organisation in the bottom-up formation of nanostructured interfaces in liquid environment and self-assembled deposition of nanoparticles from colloidal suspension play a predominant role.

The 'bottom up' approach is a new paradigm for synthesis in the nanotechnology world that could revolutionize the way the materials are made. Instead of starting with large materials and chipping away to reveal small materials, the bottom up approach starts with atoms and molecules and creates larger (but not too large!) nanostructures. The bottom up approach requires a thorough understanding of forces of attraction, which holds the particles together when they were at nano regime. The simplest such bottom up

synthesis route is electroplating. By inducing an electric field with an applied voltage, the charge particles can attract to the surface of a substrate where bonding will occur. Most nanostructured metals with high hardness values are created with this approach. It has already been proven that electroplating creates a material layer-by-layer, atom-by-atom.

Chemical Vapor Deposition is another well-known method among chemists. Using a mixture of volatile gases and taking advantage of some simple thermodynamic principles, it is possible to have your source material migrate its way to the substrate and then bond to the surface due to high chemical potentials. This is the one proven method for creating nanowires and carbon nanotubes. It is also a method of choice for creating quantum dots. Right now, CVD is the most popular and readily available method for creating nanostructures of all kinds.

Self-assembly promises to be the revolutionary new way of creating materials from the bottom up. With this method, the nanoparticle will self-organize into 2D arrays while the chemical is being evaporated from the surface. One way to achieve self-assembly is through physical attractive forces such as electricity, Van der Waals forces, and a variety of other short-range attractive forces, which can be used to orient constituent molecules in a regular array. This method has proven very effective in creating large grids of Silver (Ag), Gold (Au) in a proven periodic lattice.[32]
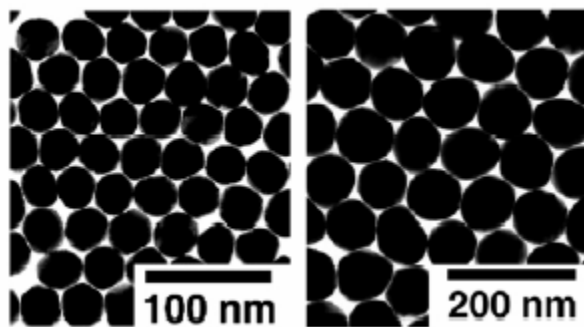
Figure 5.1 TEM images (Philips EM-400, 80 keV) of self-organized 2D arrays of 34

±2nm(left) and 87 ± 7 nm(right) Au nanoparticles stabilized by resorcinarene. The

arrays were formed at the air-water interfaceand transferred onto Formvar-coated Cu

grids.[32]

5.1.1 LASER ABLATED FILM GROWTH ON NANOTEMPLATES

The two-dimensional nanotemplates created in the previous step will selectively

promote crystalline growth of the plume material (TiC) on the hot nanospheres, with

intervening amorphous grain boundaries in the cooler regions on the substrate. This will

result in the transference of the nanotemplate pattern to the nucleation of an ordered array

of crystalline regions with grain boundaries defined by initial size of the nanoparticles on

the template. Subsequent deposition on this nanocrystalline pattern on the substrate will

lead to the vertical, self- aligned growth of nanocolumns of the crystalline material with

intervening grain boundaries (see fig 5.2). The lateral dimension of the crystalline grains

and their positions will be controllable on the nanoscale, while the coatings could

potentially be several microns thick, with large-area two-dimensional coverage on the

substrate. This technique will therefore lead to a manufacturing process for nanograined

coatings that integrates nano, micro- and meso-scale features.

5.1.2 PULSE LASER DEPOSITION (PLD)

The principle of pulsed laser deposition (PLD) is quite simple. A highly intense UV laser beam is focused on a target where the high energy density during the laser pulse (about 1 GW within 25 ns) ablates almost any material. The ablated material forms plasma, which is deposited on a substrate opposite the target. This method is quite flexible in preparing films under a wide range of deposition conditions such as kinetic energy, deposition rate and ambient gas. The advantages of the PLD method are flexibility, fast respond, energetic evaporants, and congruent evaporation. This method is particularly suited for the growth of tribological coatings since films deposited from highly excited and ionized species promote high densities. A schematic diagram of a standard PLD system is shown in fig 5.2. The disadvantages are the limited area of film growth and presence of micron sized particulates.
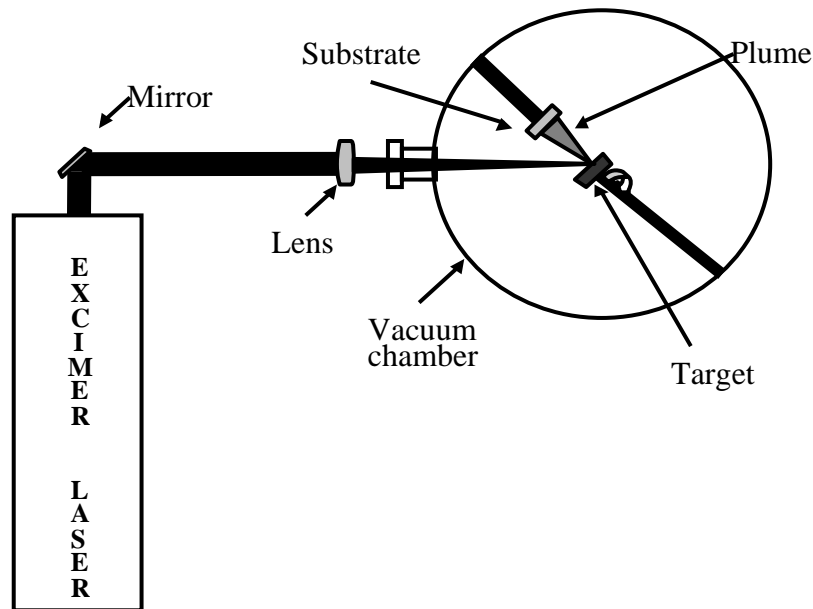
Figure 5.2: A schematic diagram of a standard PLD system.

5.2 PROCEDURE

5.2.1 SUBSTRATE PREPARATION FOR GOLD SYNTHESIS

Silicon substrates were cleaned by chemical solvent an outlined in chapter 2. In addition, solvent cleaned substrates were cleaned in piranha solution. The piranha solution is made by 1:3 H_2SO_4: H_2O_2 solutions heated up to 60^0C for 10 minutes. [Caution! This solution contains strong oxidizing agents, which cause severe burns in contact with skin and react violently with organic compounds. Storage after use should be avoided and great care and appropriate protective clothing must be employed when handling this mixture.]

5.2.2 SYNTHESIS OF GOLD NANOPARICLE 2D COATING

The procedure for the formation of gold nanoparticles is referred to as the Turkevich method. In this method particles were precipitated in solution by a chemical reaction between $HAuCl_4$ and sodium citrate

Tetrachlorauric acid (99.99%, HauCl4, 3H2O) and Citrate trisodium (95%, C6H5O7Na, 2H2O) was purchased from Alfa Aesar. A solution of 95ml of gold tetrachlorauric acid, with a weight content of 5mg of gold, was heated until boiling point under vigorous stirring. Then 5ml of a 1% sodium citrate aqueous solution was added. The solution was then stirred and kept at boiling condition for another 45 minutes. After the introduction of the citrate solution, a purple color appeared which then turned ruby red.

Drop casting technique was used to form the self-assembled nanotemplate. A drop of aqueous gold suspension was placed on a solvent-cleaned Si substrate. Most of the

particles are retained on the surface of the drop, due to the surface tension. The

surfactants prevented agglomeration and forced them to self- assemble into a two-

dimensional network. As the solvent evaporated, the particles settled on the substrate

forming 2-D template. Typically, it takes overnight to evaporate aqueous part of the

solvent and produce a light yellow color layer on the substrate.
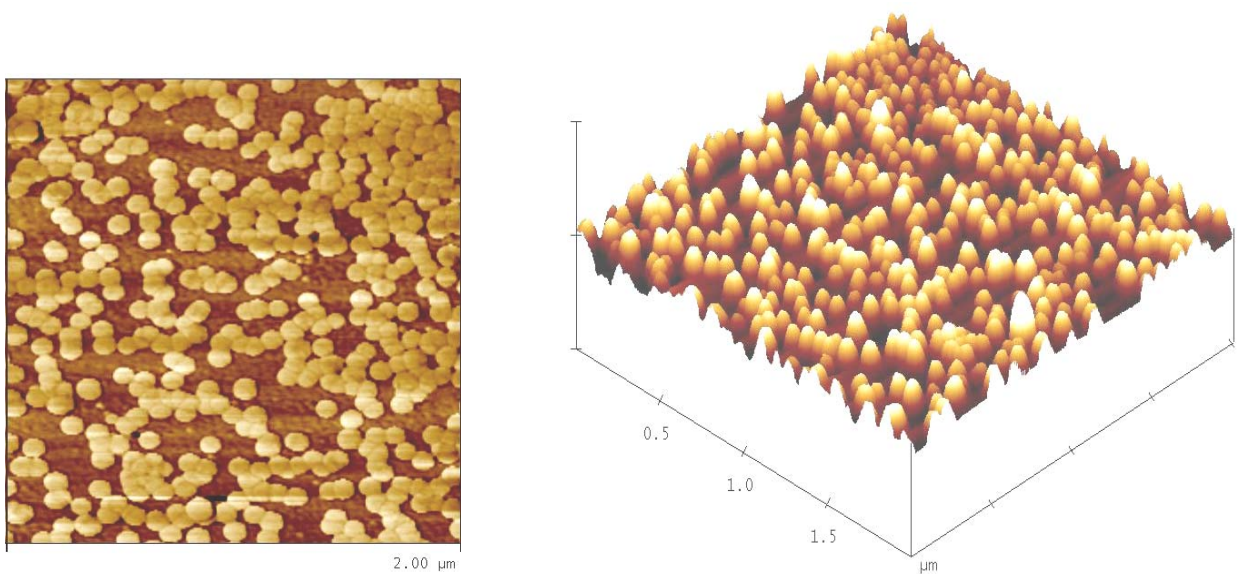

Figure 5.3 2D and 3D AFM images of gold nanoparticles on a silicon substrate before
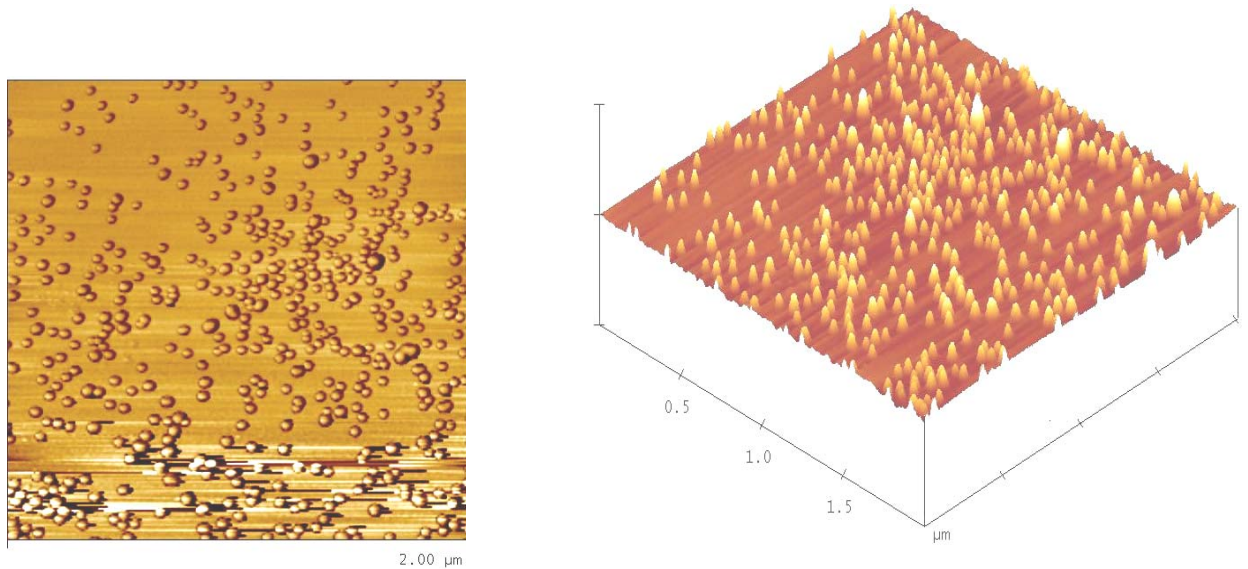
annealing.

Figure.5.4 2D and 3D AFM images of gold nanoparticles on a silicon substrate after annealing to 500 ^{0}C.

In the figure 5.3 before annealing the sample, the top right end of the images shows that the particles are arranged in such a way as to form a monolayer network. The particles touch each other without any agglomeration. The particles appear to be the same size and shape. The sizes of the particles are in the range of 80 to 90nm in diameter.

In the figure 5.4 after the annealing at 500 ^{0}C, the particle sizes have decreased. The particle sizes are in the range of 40 to 60nm. This is to be expected since heating removes the surfactants that coat the particles. Some evaporation of Au may also have taken place.

5.3 DEPOSITION OF TiC ON GOLD NANOPARTICLES

A sample made by above method was washed in deionizied water, and dried with nitrogen, and placed on a heating block in a deposition chamber. A TiC target was ablated by a KrF excimer laser at the wavelength of 248nm to deposit a film on the heated substrate. The process was run for 30 minutes by keeping substrate temperature at 500^0C and a base pressure at 10^{-6} Torr.

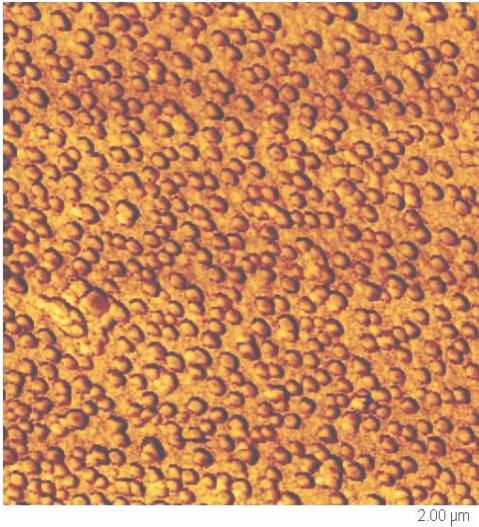Figure.5.5 2D AFM images of TiC film on gold nanoparticles

The figure 5.5 shows the images of Gold monolayer after deposition of TiC. The distance between particles and the size of the TiC particles are more defined and most of them are lying in the diameter range of 50 to 60nm. It is clear from this AFM that the TiC crystallites have preferentially nucleated on Au nanoparticles to produce a nanograined film.

CHAPTER 6

CONCLUSION

6.1 LASER ASSISTED SPRAY PYROLYSIS

In both TiC and Fe_3O_4 synthesis, we have incorporated a CO_2 laser into a chemical spray pyrolysis system to heat the droplets of an organometallic precursor dissolved in a volatile organic solvent. The drops with average diameter of 1.5μm in a narrow size distribution were generated by an ultrasonic nebulizer. The experiments have shown that when the droplets were directly incident on the substrate, they initially flatten on the surface, followed by evaporation of the solvent and decomposition Leading to large grains. When the droplets are heated up prior to incidence on the heated substrate, most of the solvent is evaporated, leading to solid particles impinging on the substrate that led to reduced the particle size. By controlling the concentration of the precursor, a further reduction in a particle size is observed. Since the laser radiation is absorbed into the carrier gas, resonance absorption by precursor is not important. Therefore this technique can be extended to any organometallic compound that can be dissolved in a volatile solvent.

6.2 TiC GROWTH ON GOLD NANOPARTICLES

In the Gold nanoparticle synthesis by Turkevich method, the resultant particle size and shape in the aqueous suspension was mainly dependent on the concentration of sodium citrate. In the presence of sodium citrate, the gold particle size is smaller and the particle size decreases with an increase in the concentration of sodium citrate. The sodium citrate serves not only as a surfactant but also as a stabilizer for nanoparticles, to prevent their further growth.

Dropcasting method has been successfully used to form 2D arrays of Au particles. Also it was indicated that the surface treatment of substrate is very important in the self-assembly of gold particles as a 2D array. Therefore, Piranha solution helps to functionalize the substrate to promote adhesion of the gold nanoparticles. The adhesion of gold particles is most probably due to interfacial electrostatic interaction between the positive charge, by the silicon lattice and citrate anions attached to the gold nanoparticles.

In the sample in PLD ablation, the TiC nano particles are likely to grow on gold nanoparicles rather than on the naked substrate. Then the sizes of the TiC particles are mainly dependent on the size of the gold nanograin on the substrate. This work also demonstrated the possibility of using the Au nanoparticles that are attached to the substrate as nucleation sites for the growth of TiC. By controlling the size of the Au particles, it may be possible to control the size of the TiC grains.

66

REFERENCES

1. Williams, W. S., Schaal, R. D. *J. Appl. Phys*. 33, 889, **1962**.

2. Jana, N. R., Gearheart L., Murphy, C. J. *J. Phys. Chem. B*. 105, 4065, **2001**.

3. Yonezawa, T., Yasui, K., Kimizuka, N. *Langmuir.* 17, 3050, **2001**.

4. Burshtain, D., Zeiri, L., Efrima, S. *Langmuir*. 15, 3050, **1999**.

5. Remita, H., Khatouri, J., Treguer, M., Amblard, S., Belloni, J. Z. *PhysD.,At, Mol., Z, Chusters*, 40, 127, **1997**.

6. Turkevich, J., Miner, R. S., Babenkova, L. *J Phys. Chem*. 90, 4765, **1986**.

7. Henglein, A. *J. Phys. Chem*. B. 104, 29, 6683, **2000**.

8. Turkevich, J. *Science*. 28, 873, **1970**.

9. Lyan, A. L., Pena, D. J., Natan, M. J. *J. Phys. Chem. B*, 103, 5826-5831, **1999**.

10. Pileni, P. M. *Lungmuir*. 13, 3266-3276, **1997**.

11. Jun Lin, C., Zhou, W., Charles, J., Conner, O. *Material Letter*. 49, 282-286, **2001**.

12. Shang, C. H. *et al.,J . Mater. Res*. 15, 835, **2000**.

13. Seitz, O., Chehimi, M. M., Deliry, E. C., Truong, S., Felidj, N., Perruchot, C., *Coll. & Surf. A: Physicochem. Eng. Aspect*. 218, 225-239, **2003**.

14. Liu, F., Chang, Y., Fu-Hsiang Ko, Tieh-Chi Chu, Bau-Tong Dai, *Microelec. Eng*. 67-68, 702-709, **2003**.

15. Chandhury, M. K., Whitesides, G. M., *Science*. 225, 1230, **1992**.

16. Haidara, H., Mougin, K., Schultz, J., *Langmuir*. 16, 9121, **2000**.

17. Rossnagle, S. M., *J Vac. Sci. & Technol. A*, 21(5), S74, **2003**.

18. Hara, T., Toida, H., *Electrochem. Solid-state Lett*. 5(10), C102, **2002**.

19. Hyun, K. K., Taylar, P. R., Lee, H. L., *Plasma Chem. & Plasma Proc*. 23(2), 223, **2003**.

20. Gomez-Dasa, O., Garica, V. M., Nair, M. T. S., Nair, P. K., *Appl. Phys. Lett*. 68(14), **1987-1996**.

21. Conde-Gallardo, A., Guerrero, M., Castillo, N. Fragoso, R., Morene, J. G., *Thin Soild Films*, Vol 473, Issu 1, 68-73, **2004**.

22. Andy Round*, H.H. Wills Physics Laboratory, University of Bristol, Bristol, BS8 1TL, UK.*

23. Pierson, H. O., Noyes, N. J., *Handbook of Chem. Vap. Deposition*.**1992**.

24. Rist, O., Murray, P. T., *Mater. Lett*. 10, 323, **1991**.

25. Abe, T., Murakami, Y., Obara, K., Hiroki, S., Nakamura, K., Mizoguchi, T., Doi, A., Inagawa, K., *J Nucl. Mater*. 133, 754, **1985**.

26. Platonov, G. L., Anikin, V. N., Anikecv, A. I., Toropchenov, V. S., Cheburaeva, R. F., *Sov. Powder Metall. Met Ceram*, 21, 889, **1983**.

27. Alexander, W., Beomseok, K., Sterphen, V. P., Steven, L. P., Balasubramanian, R., *J Inclusion Phenomena and Macrocyclic Chem* 41, 83–86, **2001**.

28. Morancho, R., Constant, G., Ehrhardt, J. J., *Thin Solid Films*, 77, 155, **1981.**

29. Takahashi, T.,Sugimaya, K., Itoh, H., *This Jl of Electrochem. Soc*. 117, 541, **1970**.

30. Wolf, S. A., Treger, D. *IEEE Trans. Mag*. 36, 2748, 2000.

31. Condon, N. G., Leibsle, F. M., Parker, T. M., Lennie, A. R., Vaughan, D. J.,and Thornton, G. , *Phys. Rev.* B. 55, 15885, 75, **1997**.

32. Hui Liu, Jiang, E. Y., Bail, H. Y., Zheng, R. K., and Zhang, X. X, *J. Phys. D: Appl. Phys.* 36, 2950–2953, **2003**.

33. Muller, K.,Herlin-Boime, N., Tenegal, F., Armand, X., Berger, F., Flank, A. M., Dez, R., Muller, K., Bill, J., Aldinger, F., *J European Ceramic Soc*. 23, 37, **2003**.